



ANNUAL  
REVIEWS **Further**

Click [here](#) to view this article's online features:

- Download figures as PPT slides
- Navigate linked references
- Download citations
- Explore related articles
- Search keywords

# Anisotropic Particles in Turbulence

Greg A. Voth<sup>1</sup> and Alfredo Soldati<sup>2,3,4</sup>

<sup>1</sup>Department of Physics, Wesleyan University, Middletown, Connecticut 06459;  
email: gvoth@wesleyan.edu

<sup>2</sup>Institute of Fluid Mechanics, Technische Universität Wien, 1060 Wien, Austria;  
email: alfredo.soldati@tuwien.ac.at

<sup>3</sup>Dipartimento Politecnico, Università di Udine, 33100 Udine, Italy

<sup>4</sup>CISM, 33100 Udine, Italy

Annu. Rev. Fluid Mech. 2017. 49:249–76

First published online as a Review in Advance on  
July 29, 2016

The *Annual Review of Fluid Mechanics* is online at  
[fluid.annualreviews.org](http://fluid.annualreviews.org)

This article's doi:  
10.1146/annurev-fluid-010816-060135

Copyright © 2017 by Annual Reviews.  
All rights reserved

## Keywords

dispersed flows, multiphase flows, turbulence, anisotropic particles, fibers, disks, rotation, preferential orientation

## Abstract

Anisotropic particles are common in many industrial and natural turbulent flows. When these particles are small and neutrally buoyant, they follow Lagrangian trajectories while exhibiting rich orientational dynamics from the coupling of their rotation to the velocity gradients of the turbulence field. This system has proven to be a fascinating application of the fundamental properties of velocity gradients in turbulence. When particles are not neutrally buoyant, they experience preferential concentration and very different preferential alignment than neutrally buoyant tracer particles. A vast proportion of the parameter range of anisotropic particles in turbulence is still unexplored, with most existing research focusing on the simple foundational cases of axisymmetric ellipsoids at low concentrations in homogeneous isotropic turbulence and in turbulent channel flow. Numerical simulations and experiments have recently developed a fairly comprehensive picture of alignment and rotation in these cases, and they provide an essential foundation for addressing more complex problems of practical importance. Macroscopic effects of nonspherical particle dynamics include preferential concentration in coherent structures and drag reduction by fiber suspensions. We review the models used to describe nonspherical particle motion, along with numerical and experimental methods for measuring particle dynamics.

## 1. INTRODUCTION

Turbulent flows with suspended particles of nonspherical shape are a common occurrence in many industrial and natural processes. Industrial processes include pulp making and papermaking (Lundell et al. 2011), pharmaceutical processing (Erni et al. 2009), and soot emission from combustion processes (Moffett & Prather 2009). Natural processes include the dispersion of pollen species in the atmosphere (Sabban & van Hout 2011), the dynamics of icy clouds (Heymsfield 1977), and the cycle of plankton and marine snow in the oceans (Pedley & Kessler 1992). The reasons for different particle shapes range from the particular generation process (ice crystals or soot) to natural selection (pollen or plankton) and design needs (textile or pulp fibers).

The problem of anisotropic particles in turbulence is quite complicated. Beyond the complexity of turbulence and of multiphase flows with spherical particles (Balachandar & Eaton 2010), we now have to consider forces and torques that depend on particle orientation. Fully specifying a problem with nonspherical particles in turbulence requires specifying many parameters, including the forcing and boundary conditions, fluid density, fluid viscosity, particle size and shape, particle density, and particle concentration. Other factors that may be important include the particle translational and rotational diffusivity, gravitational acceleration, particle deformability, collisions, aggregation or fragmentation, non-Newtonian fluid rheology, and electrostatic forces. Critical applications often involve many of these complicating factors at once. For example, papermaking involves fiber suspensions at high concentration with interparticle forces that control floc formation (Lundell et al. 2011). Icy clouds have heavy nonspherical particles sedimenting in a turbulent environment with important effects from collisions and electric charging (Pruppacher & Klett 2010).

There are many different ways for particles to be anisotropic. Pollen grains and plankton species occur in a dazzling variety of shapes. Textile or cellulose fibers vary in their shape and rigidity. But there is a simple and rich problem at the core of nonspherical particles in turbulence: How do small ellipsoidal particles translate, orient, and rotate at low concentrations in turbulent flows? Small density-matched particles translate with the fluid, independent of their shape, so their translational motion is identical to Lagrangian fluid particles in turbulence, which have been a major research focus in the past two decades (Toschi & Bodenschatz 2009). Nonspherical particles experience torque from the fluid strain field, which leads to preferential alignment. However, in turbulent flows, the fluid strain is dominated by small scales, which have a degree of universality, so many properties of nonspherical particle motion are similar between different turbulent flows. The case of homogeneous isotropic turbulence provides an important reference case in which well-defined velocity gradient statistics along Lagrangian trajectories (Meneveau 2011) produce well-defined properties of anisotropic particle motion. The close connection between nonspherical particle motion and the small scales of turbulence has also allowed studies of particle motion to produce new insights into the dynamics of fluid turbulence (Ni et al. 2014, Kramel et al. 2016). In many flows, particles become aligned by the mean velocity gradients, leading to preferential orientation (Parshah et al. 2006). Turbulent channel flow has been a particularly important case that is relevant to industrial flows and is accessible to high-resolution numerical simulations (Zhang et al. 2001). When nonspherical particles are not density matched, they exhibit many features of inertial particles in turbulence, such as preferential concentration, but with rich additional phenomena due to particle orientation and rotational slip (Mortensen et al. 2008b; Marchioli et al. 2010, 2016).

In this review, we focus on ellipsoidal particles. The fluid torques on ellipsoids are mathematically tractable, and the torques on small particles with many other shapes are the same as their equivalent ellipsoids (Jeffery 1922; Bretherton 1962; Brenner 1963; 1964a,b,c; Harris & Pittman 1975). Much of the previous work in this field has considered axisymmetric ellipsoids, also called

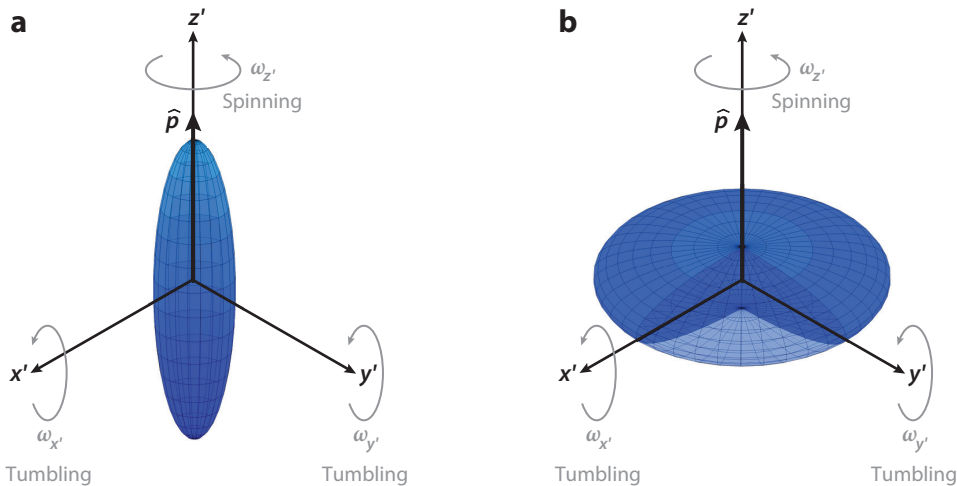


**Figure 1**

Spheroid shapes used to investigate the dynamics of anisotropic particles with  $\mathbf{p}$ , the unit vector along their symmetry axis, and their possible rotations. (a) Prolate ellipsoids,  $\lambda > 1$ , mimic the behavior of rigid rods or cylinders. (b) Oblate ellipsoids,  $\lambda < 1$ , mimic the behavior of rigid disks.

spheroids. Any spheroid shape can be specified by a single aspect ratio,  $\lambda$ , defined as the ratio of the dimension along the symmetry axis to a perpendicular dimension:  $\lambda = 1$  corresponds to a sphere,  $\lambda > 1$  corresponds to a prolate spheroid or fiber (**Figure 1a**), and  $\lambda < 1$  corresponds to an oblate spheroid or disk (**Figure 1b**). The rotations of axisymmetric particles are naturally decomposed into a component along the symmetry axis, called spinning or drilling, and components perpendicular to the symmetry axis, called tumbling.

To provide a concrete example of the rich dynamics of a small nonspherical particle in turbulence, we can examine the trajectory of a small rod in a recent experiment (Parsa et al. 2012). With the aid of high-speed imaging from multiple cameras, the Lagrangian trajectory of the rod in a nearly homogeneous turbulence field was measured and rendered in a perspective three-dimensional (3D) view (**Figure 2**). The trajectory exhibits several important features of anisotropic particles in turbulence. First, there are regions of the trajectory with very rapid changes in the particle orientation, with squared tumbling rates up to 30 times the mean square. These rare events come from intermittent large velocity gradients, which are a characteristic feature of high-Reynolds number turbulent flows. With anisotropic particles, their effects are directly evident in particle rotations. Second, the upper left section of the trajectory shows the particle spinning in a vortex with a low tumbling rate. This reflects the tendency of nonspherical particles to preferentially orient themselves with a long axis aligned with the fluid vorticity. Preferential alignment is responsible for many interesting features of nonspherical particles in turbulence.

This article reviews the status of our understanding of the complex interaction between anisotropic particles and turbulent fluid flows. We focus on the foundational problem that can be rigorously addressed using Lagrangian approaches to Kolmogorov-scale particles. Extensions to more complex cases, including the macroscopic features of multiphase flows of nonspherical particles, are also discussed. Section 2 reviews mathematical models widely used to describe kinematics and the dynamics of anisotropic particles, as well as the forces and torques acting between particles and the fluid. We examine methods used in numerical simulations in Section 3 and those used in experimental investigations in Section 4. Section 5 reviews work related to small-scale

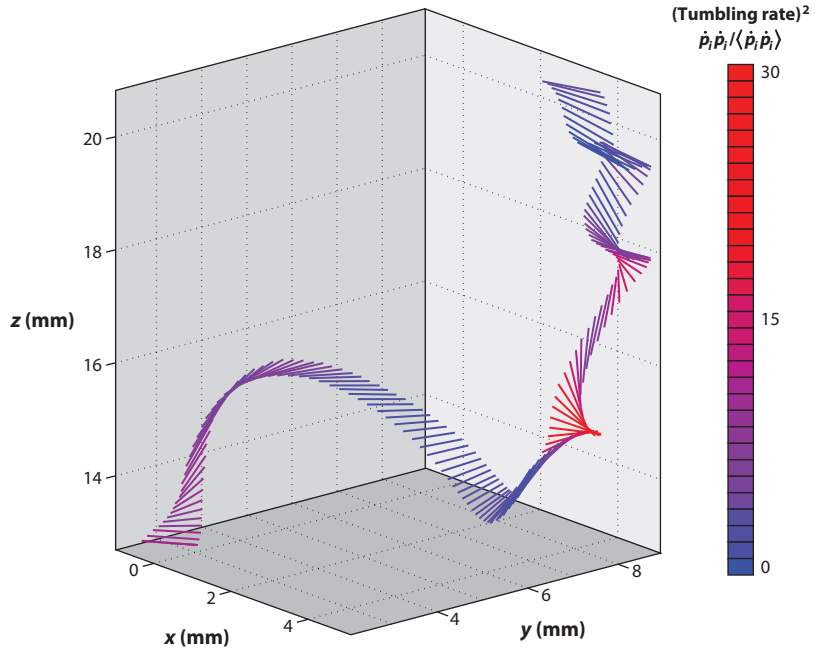


**Figure 2**

Trajectory of a fiber from multiple-camera high-speed video measurements in a turbulent flow between oscillating grids at  $R_\lambda = 214$ . The color of the rod represents the tumbling rate, with blue representing a low tumbling rate and red a high tumbling rate. The fiber has a length  $L = 1$  mm and aspect ratio  $\lambda = 5$ . Figure adapted with permission from Parsa et al. (2012).

phenomena such as preferential orientation, rotational dynamics, and relative motion between particles and fluid. Section 6 highlights a few of the profound macroscopic effects produced by collective particle motion, including preferential segregation and turbulent drag reduction.

## 2. MODELING MOTION OF ANISOTROPIC PARTICLES

**Figure 3** identifies some of the different models used to describe particle translation and rotation in turbulent flows. The particle size, particle shape, and particle to fluid density ratio are the parameters in this case. The widely used models of spherical particles are appropriate only for a narrow range of particle shapes near  $\lambda = 1$ . In the limit of high aspect ratios, a class of models derived from slender body theory has been successful (Khayat & Cox 1989, Shin & Koch 2005). At other aspect ratios, the appropriate model depends strongly on the ratio of the particle size to the Kolmogorov length scale,  $L/\eta$ , and also on the particle density. Here  $L$  is the largest dimension of a particle. The quantitative determination of the parameters at which specific models begin to fail depends on the quantities of interest and the degree of accuracy required, so we emphasize that **Figure 3** is intended for conceptual use.

### 2.1. Tracer Particles

The simplest particles to model are those that are small enough to act as perfect flow tracers. Spherical tracer particles have a velocity,  $\mathbf{u}^{(p)}$ , that matches the fluid velocity at the particle position,

**Kolmogorov scales:** the small scales of turbulence are characterized by the Kolmogorov length  $\eta = (\nu^3/\epsilon)^{1/4}$  and Kolmogorov time  $\tau_\eta = (\nu/\epsilon)^{1/2}$ , with  $\nu$  the kinematic viscosity and  $\epsilon$  the energy dissipation rate per unit mass

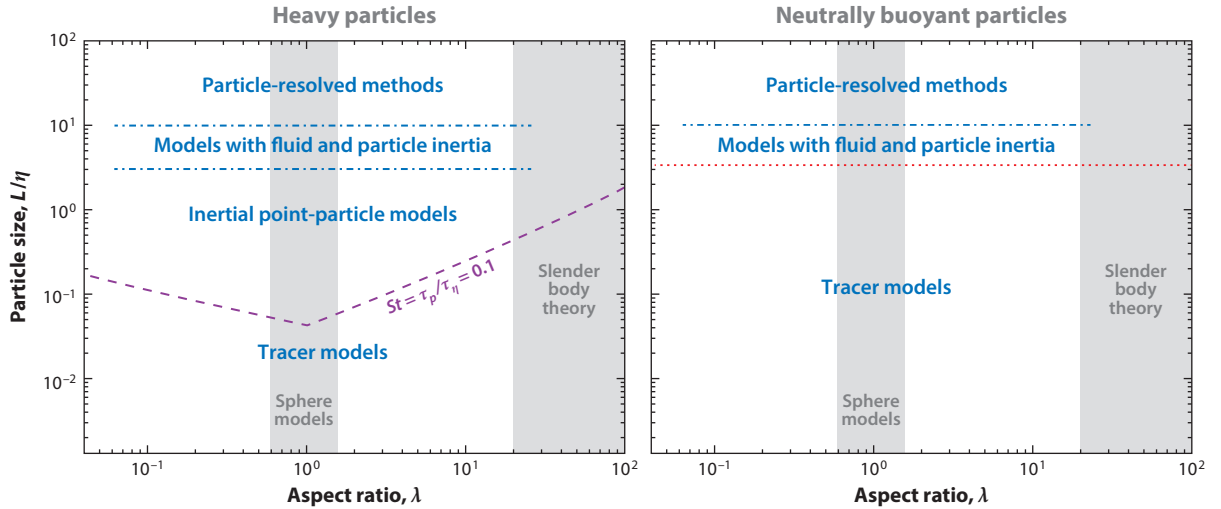


**Figure 3**

A parameter space of anisotropic particles in turbulent flows with models used to describe different cases. In this conceptual scheme, heavy particles roughly represent solid particles in air,  $\rho_p/\rho_f \sim 1,000$ . The purple dashed line is  $St = \tau_p/\tau_\eta = 0.1$  using the relaxation times given in the sidebar Particle Relaxation Times. The red dotted line is approximately the point at which tracer models begin to fail for the second moment of accelerations of spheres (Brown et al. 2009) and rotations of slender rods (Shin & Koch 2005). The blue dotted-dashed lines are simply conceptual dividers.

$\mathbf{u}^{(f)}$ , and the particle rotates at the fluid rotation rate, which is half the local fluid vorticity. Nonspherical tracer particles translate with the fluid, just like spherical particles, but their rotation depends on their orientation with respect to the velocity gradient tensor. An axisymmetric particle with symmetry axis given by the unit vector  $\mathbf{p}$  rotates with a solid-body rotation rate  $\mathbf{\Omega}$  that can be split into a spinning rate,  $\mathbf{\Omega}_p = \mathbf{\Omega} \cdot \mathbf{p}$ , and tumbling rate,  $\dot{\mathbf{p}} = \mathbf{\Omega} \times \mathbf{p}$ , so that  $\mathbf{\Omega} = \mathbf{\Omega}_p \mathbf{p} + \mathbf{p} \times \dot{\mathbf{p}}$  and  $|\mathbf{\Omega}|^2 = \mathbf{\Omega}_p^2 + |\dot{\mathbf{p}}|^2$ . For axisymmetric tracer particles, the spinning rate is half the component of the fluid vorticity along the particle axis. But the tumbling rate has a contribution from the strain rate and is given by

$$\dot{p}_i = W_{ij} p_j + \frac{\lambda^2 - 1}{\lambda^2 + 1} (S_{ij} p_j - p_i p_k S_{kl} p_l), \quad (1)$$

where  $S_{ij} = \frac{1}{2}(A_{ij} + A_{ji})$  is the strain-rate tensor and  $W_{ij} = \frac{1}{2}(A_{ij} - A_{ji})$  is the rotation-rate tensor, which are, respectively, the symmetric and antisymmetric parts of the velocity gradient tensor,  $A_{ij} = (\partial u_i)/(\partial x_j)$ . The last term in Equation 1 is the contribution parallel to  $\mathbf{p}$  needed to keep the strain from changing the magnitude of  $\mathbf{p}$ . Analysis of tracer particle rotation can be simplified by considering the equation linear in  $\mathbf{p}$  that is obtained by ignoring the last term and separately handling the normalization (Szeri 1993, Wilkinson et al. 2010). The extension to nonaxisymmetric (tri-axial) ellipsoids was considered by Jeffery (1922). Chevillard & Meneveau (2013) and Einarsson (2015) provided expressions for tracer rotations in the tri-axial case.

## 2.2. Inertial Point-Particle Models: Stokes Drag

Another class of models describes cases in which the particle Reynolds number,  $Re_p$ , is small but there is translational and rotational slip between the particle and fluid (see the sidebar Particle

**Particle Reynolds number ( $Re_p$ ):**  
 $\frac{|\mathbf{u}^{(p)} - \mathbf{u}^{(f)}| L}{\nu}$ ; defined using the slip velocity relative to the fluid and largest particle dimension,  $L$

## PARTICLE RELAXATION TIMES

For spherical particles, the translational relaxation time is  $\tau_p = (2\rho_p a^2)/(9\mu)$ , where  $\rho_p$  is the particle density,  $a$  is the particle radius, and  $\mu = \rho_f \nu$  is the dynamic viscosity. For nonspherical particles, the particle translational relaxation time depends on direction, and additional rotational relaxation times may be important.

A standard approach to define a single-particle relaxation time is to assume an isotropic particle orientation distribution, in which case the average relaxation time for a prolate spheroid is

$$\tau_p = \frac{2}{9} \frac{\rho_p a^2}{\mu} \frac{\lambda \ln(\lambda + \sqrt{\lambda^2 - 1})}{\sqrt{\lambda^2 - 1}},$$

where  $a$  is the radius perpendicular to the symmetry axis (Shapiro & Goldenberg 1993). For an oblate spheroid, the average relaxation time is (L. Zhao et al. 2015)

$$\tau_p = \frac{2}{9} \frac{\rho_p a^2}{\mu} \frac{[\pi - 2 \tan^{-1}(\lambda(1 - \lambda^2)^{-1/2})]}{2(1 - \lambda^2)^{1/2}}.$$

The relaxation times for prolate and oblate spheroids reduce to the spherical result as  $\lambda$  goes to 1.

The rotational relaxation time for a sphere is  $\tau_r = \frac{2}{15}(\rho_p a^2)/(\mu)$  (Brenner 1964b). For anisotropic particles, it is possible to define the rotational relaxation time tensor via the rotational resistance tensor (Brenner 1964b, Shapiro & Goldenberg 1993). In particle coordinates, the rotational relaxation time tensor is diagonal with different timescales for spinning and tumbling, both of which are typically shorter than the translational relaxation time (L. Zhao et al. 2015, Marchioli et al. 2016).

Relaxation Times). The spherical particle version of these models is the widely used spherical Stokes drag model (Toschi & Bodenschatz 2009).

The dynamical equations of rigid-body motion govern particle translation and rotation:

$$m \frac{d\mathbf{u}^{(p)}}{dt} = \mathbf{F}, \quad (2)$$

$$\frac{d(\mathbf{I} \cdot \boldsymbol{\Omega}')}{dt} + \boldsymbol{\Omega}' \times (\mathbf{I} \cdot \boldsymbol{\Omega}') = \mathbf{N}'. \quad (3)$$

Equation 2 is written in the inertial frame of reference, but Equation 3 requires use of the particle frame of reference so that the rotational inertia tensor,  $\mathbf{I}$ , is constant in time. The frames of reference are shown in **Figure 4**. For nonspherical particles, the drag force,  $\mathbf{F}$ , is generally not colinear with the slip velocity; therefore, a translational resistance tensor,  $\mathbf{K}'$ , is needed:

$$\mathbf{F} = \mu \mathbf{R} \mathbf{K}' \mathbf{R}^T \cdot (\mathbf{u}^{(f)} - \mathbf{u}^{(p)}). \quad (4)$$

The resistance tensor for spheroidal particles,  $\mathbf{K}'$ , is available in references (e.g., Brenner 1964c, Loth 2008, Siewert et al. 2014a, Challabotla et al. 2015a). The orthogonal rotation matrix,  $\mathbf{R}$ , converts particle coordinates to comoving coordinates, and  $\mathbf{R}^T$  is its transpose. In a number of studies (e.g., Zhang et al. 2001, Mortensen et al. 2008a, Marchioli et al. 2010), the elements of  $\mathbf{R}$  have been expressed in terms of the four Euler parameters,  $q$ , and its time evolution,  $\dot{q}$ , was computed using rigid-body kinematic equations of the form  $2 \dot{q} \bar{q} = \boldsymbol{\Omega}$ , where  $\bar{q}$  is the conjugate of  $q$  (Arribas et al. 2006). Recently, Zhao & van Wachem (2013) used quaternion algebra to perform transformations between different coordinate systems based solely on the four Euler parameters, which removes the need to compute  $\mathbf{R}$  explicitly, thus improving both numerical efficiency and precision.

### Euler parameters:

constitute a unit quaternion, a vector in 4-space subject to the unit-length constraint and allow for description of finite rotations of a single rigid body

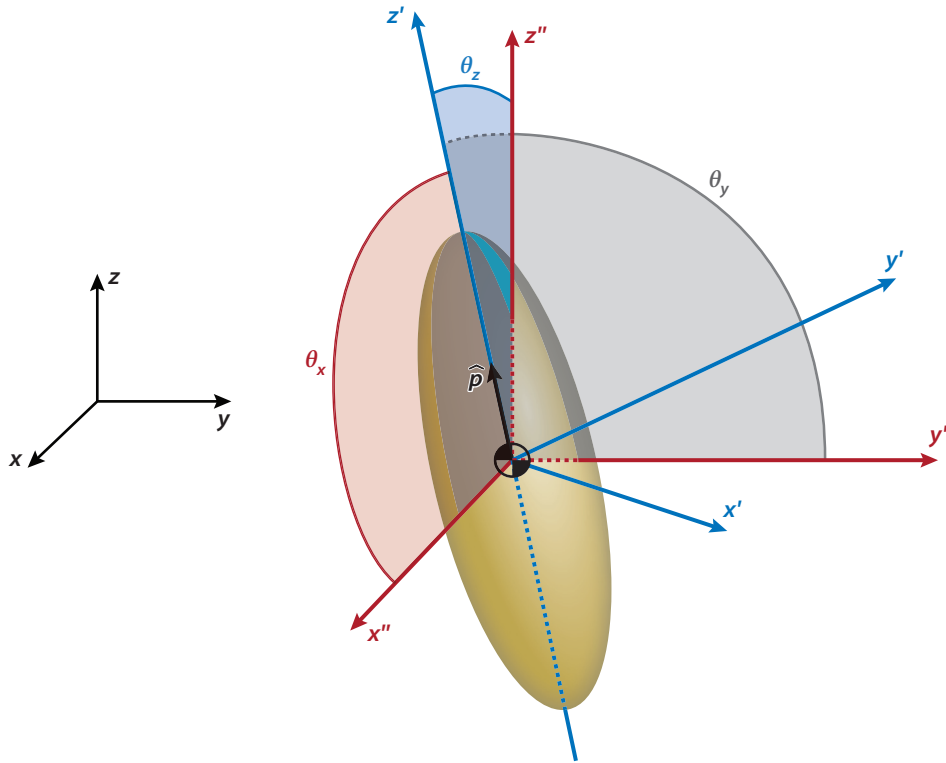


**Figure 4**

The inertial frame of reference, with axes labeled as  $x$ ,  $y$ , and  $z$ , remains fixed in space and time. The ellipsoid frame of reference, with axes labeled as  $x'$ ,  $y'$ , and  $z'$ , has its origin at the particle's center of mass and coordinate axes aligned with the principal directions of inertia of the ellipsoid. The comoving frame of reference, with axes labeled as  $x''$ ,  $y''$ , and  $z''$ , has its origin at the center of mass and is always aligned with the inertial frame of reference. The symmetry axis of the particle,  $\mathbf{p}$ , is defined to lie along  $z'$ , and its direction angles ( $\theta_x$ ,  $\theta_y$ , and  $\theta_z$ ) with respect to the inertial frame are shown.

Jeffery (1922) calculated expressions for the torques on ellipsoids,  $\mathbf{N}'$ , in Equation 3. Expressions for torque on prolate and oblate spheroids are also available in Loth (2008) and in Challabotla et al. (2015a). For particles with other shapes in creeping flow, there can be contributions to the torque from relative translation as well as from the strain rate and relative rotation (Kim & Karrila 1991, Guazzelli & Morris 2012).

### 2.3. Inertial Point-Particle Models with Fluid Inertia

In some cases, particles have all dimensions small relative to the Kolmogorov scale of the flow, but the particle Reynolds number is too large to use Stokes drag models. There are several different approaches taken in this case. The case of spherical particles is instructive. Point-particle models for small spheres in unsteady flow include the first effects of fluid inertia through added mass and Basset history terms (Gatignol 1983, Maxey 1983). Higher-order effects include Faxén and lift terms (Calzavarini et al. 2009, Meller & Liberzon 2015).

For nonspherical particles, we do not yet have analytic approaches that account for fluid inertia in unsteady flow and are applicable across the full range of spheroidal shapes. In the slender body

## ORIENTATION-DEPENDENT DRAG COEFFICIENT

On the basis of the work of Rosendahl (2000), Zastawny et al. (2012) proposed the following correlation:

$$C_D = C_{D,\phi=0^\circ} + (C_{D,\phi=90^\circ} - C_{D,\phi=0^\circ}) \sin^{a_0} \phi,$$

which allows for the prediction of the drag coefficient,  $C_D$ , as a function of the orientation,  $\phi$ , defined by the angle between the direction of the fluid velocity and the longest axis of the body. The correlation is based on the drag on the particle when parallel and perpendicular to the main flow (Leith 1987, Hölzer & Sommerfeld 2008):

$$C_{D,\phi=0^\circ} = \frac{a_1}{Re_{eq}^{a_2}} - \frac{a_3}{Re_{eq}^{a_4}}, \quad C_{D,\phi=90^\circ} = \frac{a_5}{Re_{eq}^{a_6}} - \frac{a_7}{Re_{eq}^{a_8}}.$$

The correlation is valid for a range of  $Re_{eq}$  and is a function of the nine shape-dependent coefficients  $a_i$  computed for ellipsoids, disks, and fibers (Zastawny et al. 2012, table 2). Similar correlations for the lift force and fluid torque have been proposed (Yin et al. 2003, Zastawny et al. 2012).

limit, solutions can be derived from Navier-Stokes because two dimensions are small enough that the Reynolds number of the inner flow remains low (Khayat & Cox 1989). The full range of spheroidal shapes has been studied in steady simple shear flow, leading to a fairly comprehensive picture of the effects of fluid and particle inertia in that case (Ding & Aidun 2000, Subramanian & Koch 2005, Einarsson et al. 2015, Rosén et al. 2015, and references therein).

Empirical drag models have been developed to address many applied problems in which non-spherical particles have larger particle Reynolds numbers (e.g., Mandø & Rosendahl 2010, Raman & Fox 2016). The familiar drag coefficient for a sphere can be found in any fluids textbook (e.g., Bird et al. 1960) as a piecewise approximation fitted to a large amount of experimental data.

Drag coefficient data exist for cylinders and disks in a fixed orientation in a laminar flow (e.g., Lapple & Shepherd 1940). Some experimental data exist for anisotropic particles (Haider & Levenspiel 1989), but in the case of ellipsoids, there is an apparent lack of investigation (El Khoury et al. 2010). Modeling efforts (Rosendahl 2000, Yin et al. 2003) and computational efforts (Hölzer & Sommerfeld 2008; Zastawny et al. 2012; Jiang et al. 2014, 2015) have collected data for lumped drag coefficients in the cases of ellipsoids in shear or uniform flow at different orientations. Expressions for the drag coefficient of different aspect ratios at any orientation have been developed and benchmarked (Ouchene et al. 2015) (see the sidebar Orientation-Dependent Drag Coefficient). Loth (2008) presented an analysis based on trajectory-averaged drag coefficients using the approach of Ganser (1993) in expressing the drag force as a function of the particle Reynolds number and shape-dependent coefficients. As remarked by Loth (2008), drag coefficients are usually given as a function of the particle Reynolds number,  $Re_{eq}$ , which is based on the diameter of the volume-equivalent sphere.

### 2.4. Large Particles

When particles have at least one dimension larger than the Kolmogorov scale, they interact with the nonlinear variation of the velocity field, and point-particle models are no longer possible. In general, large particles have been studied with particle-resolved simulations (see Section 3) and with experiments (see Section 4). The one exception is in the slender rod limit, for which Olson & Kerekes (1998) and Shin & Koch (2005) developed expressions for the response of a thin fiber to a spatially varying velocity field. Some statistical properties of the motions of very large particles in

turbulence can be modeled by considering the range of turbulent scales that affect particle motion and relating particle statistics to known statistical properties of the turbulent cascade (Parsa & Voth 2014).

---

**DNS:** direct numerical simulation

---

### 3. DIRECT NUMERICAL SIMULATION APPROACHES

Many recent developments in turbulence have been obtained by the use of direct numerical simulation (DNS) (Hussain 1983, Rogallo & Moin 1984, Moin & Mahesh 1998). Because DNS is able to solve for all scales of motion, down to the smallest, it has been particularly valuable to the study of turbulent dispersed flows, in which the limiting case of small spherical particles has received extensive attention (Elghobashi & Prosperetti 2009, Balachandar & Eaton 2010). For anisotropic particles in turbulence, the number of papers exploiting DNS to elucidate fundamental physical features is quickly growing (Soldati & Andersson 2013, Voth 2015). This section examines current modeling approaches to DNS of either small, sub-Kolmogorov particles or larger particles.

#### 3.1. Lagrangian Point-Particle Models: One-Way Coupling

Lagrangian models are based on DNS of the Eulerian velocity field and computation of the trajectory of the particles according to the equations defined in Section 2. The first contributions paving the way to Lagrangian tracking of nonspherical particles in DNS were by Mallier & Maxey (1991) and later by Shin & Maxey (1997), who investigated the combined actions of rotation, inertia, and gravity on the velocity of prolate and oblate spheroids settling in a synthetic cellular flow. In both papers, the authors used Stokes flow models for inertial particles.

Zhang et al. (2001) investigated the transport and deposition of ellipsoidal particles in a DNS of turbulent channel flow. The parameter range and quantities examined in this flow configuration have been rapidly expanded by subsequent works (Mortensen et al. 2008a,b; Marchioli et al. 2010, 2016; Moosaie 2013; Marchioli & Soldati 2013; L. Zhao et al. 2015). The one-way coupling approach provides a formally clean framework to examine in detail the influence of turbulence on particles at low particle concentration, but gives no information regarding the influence of particles on turbulence and particle-particle interactions. The main findings of these works are related to orientation and rotation statistics, which show a tendency of fibers to align in the direction of the mean flow close to the wall, and to the preferential concentration of particles. The same observables have also been evaluated in DNS of isotropic turbulence (e.g., Parsa et al. 2012, Gustavsson et al. 2014, Siewert et al. 2014a, Byron et al. 2015, and references therein), in which fiber alignment induced by the fluid velocity gradients resulted in rotation rates much lower than those predicted by rotationally averaged models.

The main assumptions characterizing the one-way coupling approach are that fibers are approximated as noninteracting ellipsoids with uniformly distributed mass immersed in a dilute flow. Additionally, the fiber size is assumed to be smaller than the Kolmogorov length scale, and lubrication forces arising when particles are in close proximity are ignored. Also ignored are aggregation and breakup phenomena. Despite these simplifications, however, the resulting lumped-parameter model captures the key physics coupling the orientation of particles to the velocity gradients and coupling the translational motion to the orientation, as highlighted in Section 2. The dependence of the hydrodynamic viscous drag force on the particle orientation creates crucial differences between elongated fibers and equivalent spherical particles. The influence of fiber inertia and shape was investigated by directly comparing fiber rotation and orientation with the local properties of

---

**LES:** large-eddy simulation

**A priori LES:** large-eddy simulation field obtained from a filtered direct numerical simulation field

---

the carrier flow in a turbulent channel (e.g., Marchioli et al. 2016, and references therein) and in homogeneous isotropic turbulence (e.g., Byron et al. 2015, and references therein).

A few studies have applied Lagrangian tracking of anisotropic particles in large-eddy simulation (LES)-resolved turbulence fields. Njobuenwu & Fairweather (2015) studied the effect of particle shape on their dynamics in an LES-resolved turbulent channel flow. They used shape- and orientation-dependent drag and lift coefficients to solve for translational and rotational motions of oblate and prolate ellipsoids. Lecrivain et al. (2016) studied the sedimentation of fibers in flat and roughened channels using quasi-DNS resolution. An intriguing suggestion of the scale separation in modeling translational and rotational motion of ellipsoids was provided by Chen et al. (2016). Using DNS, a priori LES, and LES, and following an approach similar to that used for spherical particles (Bianco et al. 2012, Geurts & Kuerten 2012), they observed that the filtered subgrid-scale fluid motions in LES flow fields have significant effects on the rotational statistics of ellipsoidal particles.

### 3.2. Two-Way and Four-Way Coupling

Even small particles will influence the fluid momentum equation when their volume fraction is high enough. Owing to preferential concentration and clustering, this can occur locally as well as globally. In dense flows, interparticle collisions may also become important, leading to aggregation or fragmentation with direct and indirect effects on the collective dynamics of the particles. Given the complexity of modeling the momentum exchange between the carrier and dispersed phase, two-way coupling studies of nonspherical particles are scarce in the literature. In Eulerian-Lagrangian simulations, momentum coupling between spherical particles and fluid is mostly done via the point-force approximation (e.g., Crowe et al. 1996, Balachandar & Eaton 2010), which usually neglects the torque coupling (Andersson et al. 2012). The computation of the stresses exerted by the rods on the fluid is not straightforward (Suen et al. 2002), possibly including the direct computation of the Fokker-Planck equation for the orientation distribution function or other methods (Szeri & Leal 1992, 1994). Combined with the large number of particle trajectories required to obtain values of stress at any point in the flow field, these computations quickly become unfeasible. Early DNS-based attempts to compute the stresses due to fibers are based on closure models (Den Toonder et al. 1997, Moosaie & Manhart 2011), on moment approximation methods (Paschkewitz et al. 2004, 2005b; Gillissen et al. 2007a,b), or on the use of Monte Carlo simulations for the conformation distribution function of the fibers (Moosaie 2013, Moosaie & Manhart 2015). In these works, fibers are assumed much smaller than the Kolmogorov length scale, their distribution remains homogeneous in the fluid, and they are able to exchange stresses with the fluid according with their local orientation.

Recently, Eulerian-Lagrangian fully coupled simulations for fibers on the order of the Kolmogorov scale in turbulent channel flow have been performed to examine the collision mechanisms of fibers with the walls (Zhao & van Wachem 2013), as well as the physics of fiber-induced turbulence modulation and its dependence on fiber length (L. Zhao et al. 2015). These aspects are investigated for semidilute concentrations considering statistical observables based either on fluid and fiber velocities (e.g., turbulent kinetic energy, fluid-fiber correlations) or on fiber orientation (e.g., direction cosines). Collision rates for dense suspensions of fibers or, more generally, nonspherical particles in channel flow have not yet been measured numerically. To the best of our knowledge, collision rates have been computed only for small ellipsoidal particles settling in decaying isotropic turbulence (Siewert et al. 2014a), with results showing the dependence of the particle orientation on the gravitational settling velocities, which determine the collision probability.

### 3.3. Finite Size and Fluid Inertia Effects

Shin & Koch (2005) first demonstrated the limits of the low-Reynolds number approximation for fiber motion by employing DNS to compute the torque acting on very slender fibers with sizes ranging from tracers that rotate like material lines to particles much longer than the Kolmogorov scale. For increasing length, rotational motions slow down, demonstrating that the particles filter the effects of the smaller eddies.

Computational approaches investigating the motion of large particles that are not in the slender body limit require accurate tracking of the particle interface and integration of fluid forces, which involve more complex algorithms and larger computational resources. The advantage of these methods is a straightforward way to overcome the limits imposed by the low-Reynolds number approximation at the basis of the point-particle Stokes flow model.

The motion of large particles has been largely investigated (Tenneti & Subramaniam 2014) by exploiting force coupling methods (Liu et al. 2009), the fictitious domain method (Pan et al. 2002), immersed boundary methods (Mittal & Iaccarino 2005), and lattice Boltzmann methods (Aidun & Clausen 2010). However, at present these computationally expensive approaches are unable to handle suspensions of millions of small finite-size particles, as often required to obtain reliable particle statistics in a turbulent flow environment. Even though these methods have indeed been used to simulate finite-size spherical particles in turbulent flow (Uhlmann 2008, Lucci et al. 2010), we can report only one investigation in the specific domain of anisotropic rigid particles in turbulence (Do-Quang et al. 2014). Using a lattice Boltzmann method, these authors were able to simulate on the order of 10,000 spheroidal particles with a size equivalent to several grid cells, including contact and lubrication force models for fiber-fluid, fiber-fiber, and fiber-wall interactions.

## 4. EXPERIMENTAL APPROACHES

Despite the ubiquity of turbulent flows with nonspherical particles, it has been only relatively recently that experiments have been developed to measure the orientation and rotation of individual particles in a turbulent environment. Early experimental work focused on particle motion in laminar flows and complex cases relevant to specific applications; however, we do not review early work here and instead refer readers to a few papers that cite this work. For example, Noel & Sassen (2005) reviewed early work on ice crystals in clouds; Bernstein & Shapiro (1994) identified early laboratory experiments that measured particle orientations; and Zhang et al. (2001) reviewed work on the deposition of nonspherical particles. Recent experimental measurements have relied almost exclusively on imaging, with most of the work imaging the motion of fibers.

### 4.1. Single-Camera Methods

Because fibers are nearly 1D, a single camera can measure the projection of the particle orientation,  $\mathbf{p}$ , onto the image plane. A small fraction of particles that point directly toward the camera cannot be measured, but this is rare for high-aspect ratio fibers, making single-camera measurements simple and effective. Parsheh et al. (2005, 2006) studied the orientation distribution of fibers in a turbulent flow as it accelerated through a planar contraction. They used 2D images of neutrally buoyant rayon fibers to determine the fiber orientation distribution. A nearly isotropic turbulent flow behind a grid produces a nearly isotropic particle orientation distribution, and they measured how the preferential orientation develops as particles experience the mean strain from the contraction. Carlsson et al. (2010) measured fiber orientations in the bulk and near-wall regions of a similar accelerating flow using a headbox geometry relevant to the paper industry. Håkansson et al. (2013) analyzed the preferential concentration of fibers in the boundary layer of a half-channel

flow down an incline. Kvick (2014) used 2D imaging to measure the orientation distribution of fibers in the boundary layer of the same flow. This work includes a section identifying nine physical parameters necessary to specify the fiber suspension flow and the five nondimensional groups they form, which highlights a theme of our review: Turbulent flows of nonspherical particles occur in a large parameter space that has just begun to be explored. Hoseini et al. (2015) extended this work to resolve the distance from the wall, with a particular focus on measuring the motion of particles within one particle length of the wall, where new physics beyond simple Stokes drag models become important. Capone & Romano (2015) and Capone et al. (2015) measured fiber concentration and orientation in the flow over a backward-facing step and in an immersed free jet.

A wide variety of methods have been developed for determining fiber orientations from 2D images. Carlsson et al. (2011) described a steerable filter that provides an accurate way to extract orientations of fibers from 2D images, and they applied it to images from a turbulent half-channel flow. Abbasi Hoseini et al. (2014) developed a neural network method for tracking fibers in successive images. A particular challenge occurs when attempting to use imaging systems to simultaneously measure fiber motion and the fluid velocity field around the particles. Various groups have developed different solutions to separate the fibers and tracers in images (Bellani et al. 2012, Dearing et al. 2013, van Hout et al. 2013, Ni et al. 2015).

A drawback of standard single-camera measurements is the missing orientation coordinate. **Figure 5** shows a comparison of mean orientations of fibers in a channel flow from single-camera experiments and DNS from Dearing et al. (2013). Close to the centerline, the particles are nearly randomly oriented in both experiments and simulations, but the measured mean orientation is different because of the projection effect. If the 3D probability distribution of orientations is

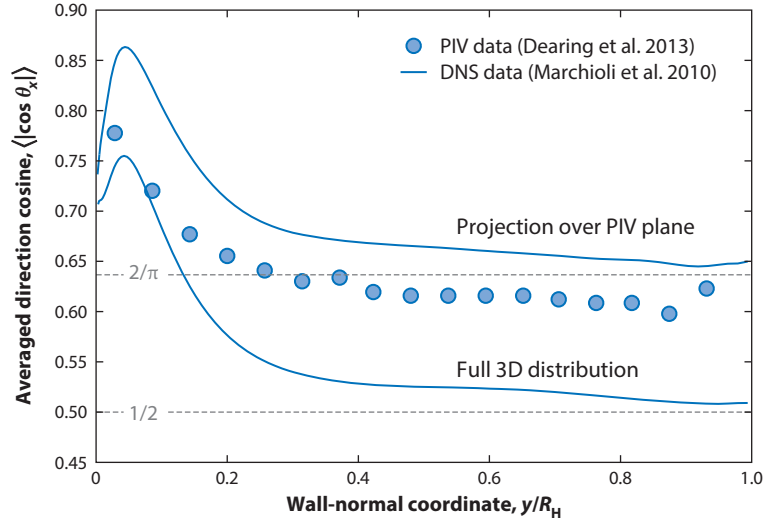


**Figure 5**

Fiber mean orientation as a function of distance from the wall in turbulent pipe flow at  $Re_\tau = 250$ . The wall distance is scaled to the hydraulic radius,  $R_H$ . Blue symbols refer to particle image velocimetry (PIV) experimental data taken in a 10-cm pipe, and the solid lines refer to direct numerical simulation (DNS) data for channel flow (Marchioli et al. 2010). Dashed lines indicate the average direction cosine of a full 3D isotropic distribution ( $\langle \cos \theta_x \rangle_{3D} = 1/2$ ) and average direction cosine of the projection over the camera measurement plane of a full 3D isotropic distribution ( $\langle \cos \theta_x \rangle_{2D} = 2/\pi$ ).

known, the mean can be corrected. Away from the centerline, the 3D distribution is not known in the experiments, and comparison requires projecting the DNS data onto the plane accessible to the experiments.

A powerful method for obtaining 3D particle orientations from single-camera measurements is digital holography. van Hout et al. (2013) described an implementation of this method for fiber tracking. They noted that multiple-camera holographic systems are needed to obtain high position resolution in all directions.

## 4.2. Multiple-Camera Methods

Multiple cameras allow the full fiber orientation vector to be measured at the cost of more complex camera calibration (Bernstein & Shapiro 1994, Parsa et al. 2012, Parsa & Voth 2014). With three cameras whose viewing axes are not in the same plane, the full 3D orientation can be measured for any particle orientation. The use of more than three cameras improves the robustness of orientations measured from messy images, which are the norm in turbulent imaging applications.

Recently, multiple-camera methods have been extended to measure the orientation and rotation rates of particles with more complex shapes. Bellani et al. (2012) developed methods for injection molding particles from hydrogel, which are transparent, are index matched to the fluid, and have tracers embedded in them. They used a stereoscopic particle image velocimetry system with a laser sheet much thinner than a hydrogel particle. The measurements provide three component velocity fields in both the fluid and solid phase with sufficient resolution to measure many velocity vectors on a sheet inside a single hydrogel particle. From these velocities, they obtain measurement of the full solid-body rotation rate vector of the particle. This method has been used in more recent work (e.g., Bellani et al. 2013, Byron et al. 2015).

Marcus et al. (2014) used 3D printed particles to measure the orientation and rotation of particles with shapes made of many slender arms, which allow them to study effective ellipsoids across a range of aspect ratios. To measure the orientation of these particles from multiple-camera images, they developed a general method that projects a model particle onto each camera. A least-squares minimization of the difference between the model and experimental images provides the position and Euler angles that best match the measured images.

## 4.3. Other Experimental Methods

There are a variety of other experimental methods used for suspensions of complex particles. In this review, we focus on fundamental dynamics at lower concentrations, but at higher concentrations, these suspensions typically become opaque, and methods such as nuclear magnetic resonance, optical coherence tomography, acoustic velocimetry, and capacitance tomography need to be used to see inside the sample. None of these is currently able to track small single-particle orientations, but high concentration will continue to be an important case, and these methods or particle-fluid index matching (Holm & Soderberg 2007) is necessary for measurements. Experimental tools for optical imaging as well as these other measurements continue to improve rapidly, and we are likely to see new regions of parameter space opened up to precision measurements in the years to come.

## 5. STUDIES OF ALIGNMENT AND ROTATION OF NONSPHERICAL PARTICLES

In this section, we review some of the main scientific results obtained in studies on the orientation and rotation of nonspherical particles at low concentrations in turbulence.

---

**Euler angles:**  
the three subsequent rotations required to rotate from the ellipsoid reference frame to the inertial reference frame

---

## 5.1. Preferential Orientation

A central focus of work on anisotropic particles in turbulence has been on understanding the probability distribution of the particle orientation,  $\psi(\mathbf{p}, \mathbf{x}, t)$ . Alignment is often quantified using the moments of the orientation distribution (Hinch & Leal 1975):

$$a_{ij} = \langle p_i p_j \rangle = \int \psi p_i p_j d\mathbf{p}, \quad (5)$$

$$a_{ijkl} = \langle p_i p_j p_k p_l \rangle = \int \psi p_i p_j p_k p_l d\mathbf{p}. \quad (6)$$

There are some subtleties in exactly how the deterministic and stochastic contributions to the particle orientation distribution are defined. Often the orientation distribution is considered to have deterministic contributions from the average velocity field and stochastic contributions from turbulent fluctuations, Brownian motion, and the initial particle orientation (Krushkal & Gailly 1988). But it is also possible to consider the instantaneous orientation distribution at the location of a single fluid element with deterministic contributions from the history of the velocity gradients at the particle position and stochastic contributions from the initial particle orientation and Brownian motion (Szeri & Leal 1993).

Particles are oriented by deterministic velocity gradients and randomized by stochastic velocity gradients and Brownian effects. The relative importance of orienting and randomizing effects can be quantified by a rotational Péclet number,  $P_e = (dU/dx)/(D_p)$ , where  $dU/dx$  is a typical deterministic strain rate and  $D_p$  is the rotational diffusivity. In the Brownian case, the rotational diffusivity can be calculated (Bernstein & Shapiro 1994, and references therein). Although turbulent rotations are not simple diffusion, the particle orientation can often be described with diffusive models (Olson & Kerekes 1998, Marchioli & Soldati 2013). Shin & Koch (2005) evaluated in detail the ways to quantify the turbulent rotational diffusivity. Although some foundational work on nonspherical particles in fluid flows was inspired by the rheology of suspensions in which Brownian motion is important (Hinch & Leal 1972), we focus the rest of this review on non-Brownian particles with orientation distributions that are the result of turbulent fluctuations.

**5.1.1. Alignment in turbulent shear flows.** A widely studied case is the alignment of anisotropic particles in turbulent shear flows. Here the orientation distributions of particles are studied in laboratory coordinates, and the preferential orientation is a result of competition between alignment by mean velocity gradients and randomization by fluctuating velocity gradients. Almost all the studies that determine 3D orientations of individual particles in shear flows are numerical simulations, and most have worked with the simple case of inertial fibers without gravity. An important sequence of papers using inertial point-particle simulations in DNS of turbulent channel flow has developed a clear phenomenology concerning preferential alignment near the wall (Zhang et al. 2001, Mortensen et al. 2008b, Marchioli et al. 2010, Marchioli & Soldati 2013, Challabotla et al. 2015b, F. Zhao et al. 2015, L. Zhao et al. 2015).

**Figure 6a** shows one component of the mean orientation of neutrally buoyant particles with a range of aspect ratios in a channel flow. In the center of the channel, all particles approach random orientation. But near the wall, fibers are aligned very differently than disks. Fibers align with their symmetry axis preferentially in the streamwise direction, whereas disks align with their symmetry axis in the wall-normal direction. This alignment can be understood as a result of particles that are temporarily in Jeffery orbits (Jeffery 1922). Particles with aspect ratios very far from 1 will spend most of their time aligned in the observed preferential orientation before quickly tumbling and returning to the preferred alignment.

When the particle Stokes number increases, inertia makes some significant changes in the particle orientation, particularly for disks. **Figure 6b** shows the same mean orientation component

---

### Jeffery orbits:

periodic rotation of small neutrally buoyant axisymmetric particles in a steady viscous shear flow

### Stokes number ( $St$ ):

ratio of  $\tau_p$  to the fluid timescale; the Kolmogorov timescale is used for homogeneous flows, and the viscous timescale is used in wall-bounded turbulence

---

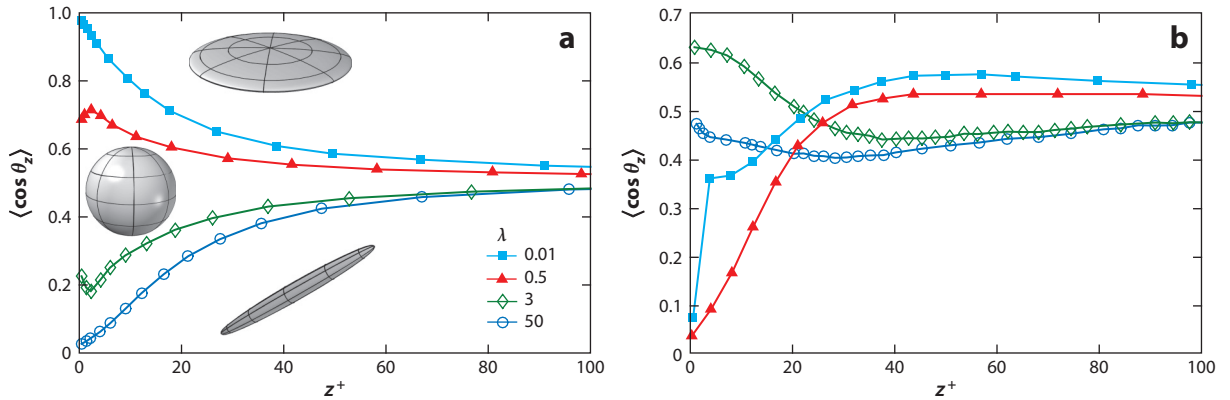


**Figure 6**

Mean wall-normal component of the particle orientation for particles of different aspect ratios from direct numerical simulation of turbulent channel flow and a one-way coupled inertial point-particle model: (a) tracer particles ( $St = 0$ ) and (b) inertial particles ( $St = 30$ ). The near-wall preferential orientation is dramatically different between tracer and inertial particles. Disks ( $\lambda < 1$ ) switch from a wall-normal to spanwise preferential orientation as the particle inertia increases. Data taken from Challabotla et al. (2015a,b) and Marchioli et al. (2010).

as in **Figure 6a**, but for particles with  $St = 30$  rather than tracers. The alignment is totally different with the disks now perpendicular to the wall-normal direction. The full published data show that these disks are spinning like wheels with  $\mathbf{p}$  in the spanwise direction. This phenomenon can also be related to particle dynamics in simple shear flow, in which particle inertia causes the degenerate Jeffery orbits to become unstable. Disks migrate toward spinning motion with  $\mathbf{p}$  in the spanwise direction, whereas fibers migrate toward tumbling motion with  $\mathbf{p}$  in the wall-normal/streamwise plane, matching the preferential orientation observed in the turbulent simulations (Rosén et al. 2015, and references therein).

For inertial particles, the preferential orientation combines with the particle slip velocity to make significant changes in the wall-normal velocities, which can have significant effects on particle deposition rates. Zhang et al. (2001) and Marchioli et al. (2010) have simulated these effects.

**5.1.2. Alignment in homogeneous isotropic turbulence.** In isotropic turbulence, there can not be any preferential alignment in laboratory coordinates, but the dynamics of anisotropic particles are still strongly affected by preferential alignment. Particles become aligned with the local velocity gradient tensor. This alignment has large effects on particle rotations, as described in Section 5.2.1. It also causes nearby particles to be instantaneously aligned with each other, which can affect light scattering and rheology.

Pumir & Wilkinson (2011) explored the alignment of slender fibers, aspect ratio  $\lambda \gg 1$ , in isotropic turbulence. They found that fibers have their symmetry axis,  $\mathbf{p}$ , strongly aligned with the vorticity vector. Alignment with the eigenvectors of the strain rate tensor is weaker, with  $\mathbf{p}$  aligned best with  $\hat{e}_2$ , slightly less with  $\hat{e}_1$ , and strongly perpendicular to  $\hat{e}_3$ . Experiments have recently been able to access both the orientations of a fiber and the velocity gradient tensor around it (Ni et al. 2015), finding alignment that is broadly consistent with the simulations. For thin disk-shaped particles,  $\lambda \ll 1$ , the symmetry axis is preferentially aligned with  $\hat{e}_3$  and perpendicular to the vorticity (Gustavsson et al. 2014, Byron et al. 2015). **Figure 7** encapsulates the preferential alignment of slender fibers and thin disks in homogeneous isotropic turbulence. The spherical

**Strain rate eigenvectors:**

mutually orthogonal eigenvectors,  $\hat{e}_1$ ,  $\hat{e}_2$ , and  $\hat{e}_3$ , traditionally ordered by their corresponding eigenvalues, with  $\hat{e}_1$  the largest (most extensional) and  $\hat{e}_3$  the smallest (most compressive)

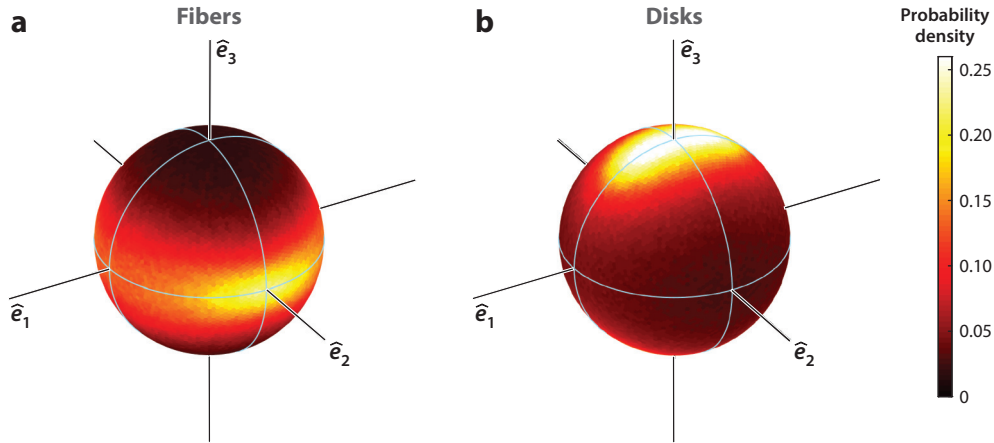


**Figure 7**

Spherical probability density functions of the orientation of (a) fibers and (b) disks in the coordinate system defined by the eigenvectors of the strain rate tensor. Axes and great circles are drawn for visual clarity. The numerical simulations are the same ones used in Parsa et al. (2012) and in Ni et al. (2015).

probability density of the particle orientation,  $\mathbf{p}$ , is shown in the coordinate system defined by the eigenvectors of the strain rate tensor.

## 5.2. Rotation Rate

The preferential alignment of nonspherical particles has profound implications for particle rotation statistics.

**5.2.1. Rotations in homogeneous isotropic turbulence.** Shin & Koch (2005) observed that the mean square tumbling rate,  $\langle \dot{p}_i \dot{p}_i \rangle$ , for slender tracer fibers advected by the flow was a factor of 2.8 smaller than predicted for randomly oriented fibers. Parsa et al. (2012) performed experiments in approximately homogeneous isotropic turbulence that agreed with the earlier simulations and also presented DNS results on the probability distribution of tumbling rates of spheroids across all aspect ratios. Marcus et al. (2014) extended the experimental tumbling rate measurements to disks and spheres. These results have very little dependence on the Reynolds number of the flow (Shin & Koch 2005, Parsa et al. 2012).

For slender fibers, the tumbling rate was the natural rotational variable to consider. However, experimental tools introduced by Bellani et al. (2012) allowed the full solid-body rotation rate of axisymmetric particles to be measured and motivated comparison of statistics of spinning and tumbling. Byron et al. (2015) studied the spinning, tumbling, and the full solid-body rotation rate of spheroids of all aspect ratios. **Figure 8** shows their data for the mean square tumbling rate as a function of aspect ratio. Both the mean square spinning rate and the tumbling rate depend strongly on the aspect ratio. They combine to produce a mean square solid-body rotation rate that is nearly independent of shape.

The alignment and rotation of small neutrally buoyant nonspherical particles have been rationalized as a consequence of the particles becoming aligned with a long axis along the direction in which the fluid has been stretched (Marcus et al. 2014, Ni et al. 2014). A counterintuitive feature of turbulent flows is that the direction in which the fluid has been stretched is preferentially aligned

with the intermediate eigenvector of the instantaneous strain rate tensor  $\hat{e}_2$ . From this empirical fact, it naturally follows that fibers should have  $\mathbf{p}$  preferentially along  $\hat{e}_2$ , whereas disks should have  $\mathbf{p}$  preferentially in the plane of  $\hat{e}_1$  and  $\hat{e}_3$ . Conservation of angular momentum causes the vorticity to also preferentially align with the direction in which the fluid been stretched. This leads to particles with a long axis aligned with the vorticity vector (Ni et al. 2014). Most features of rotations of neutrally buoyant particles can be understood in this framework. Fibers tumble slowly because they are aligned with vorticity, so it does not contribute to  $\dot{\mathbf{p}}$ . Disks preferentially have  $\mathbf{p}$  perpendicular to the vorticity, so vorticity contributes strongly to tumbling but almost nothing to spinning. Because strain cannot contribute to the spinning of axisymmetric particles, disks spin very slowly.

**5.2.2. Rotations in turbulent shear flows.** In shear flows, particle rotation has been extensively studied in laboratory coordinates. Marchioli & Soldati (2013) reported the mean and root mean square rotation statistics for inertial fibers as a function of distance from the wall. Challabotla et al. (2015a,b) provided the same statistics for disks and neutrally buoyant particles. L. Zhao et al. (2015) recently connected much of what we know about rotations in homogeneous isotropic turbulence with what we know about tracer and inertial particles in turbulent channel flow. They decomposed rotations into spinning and tumbling and observed statistics near the channel centerline that are very similar to earlier results in isotropic turbulence. The addition of particle inertia results in relatively small changes near the channel centerline, with both the spinning and tumbling rates decreasing for heavier particles. However, near the wall at  $z^+ = 10$ , the relative importance of spinning and tumbling changes dramatically. The changes are largest for inertial particles. For example, heavy disks spin much faster than heavy fibers, the opposite of the isotropic turbulence trend in **Figure 8**.

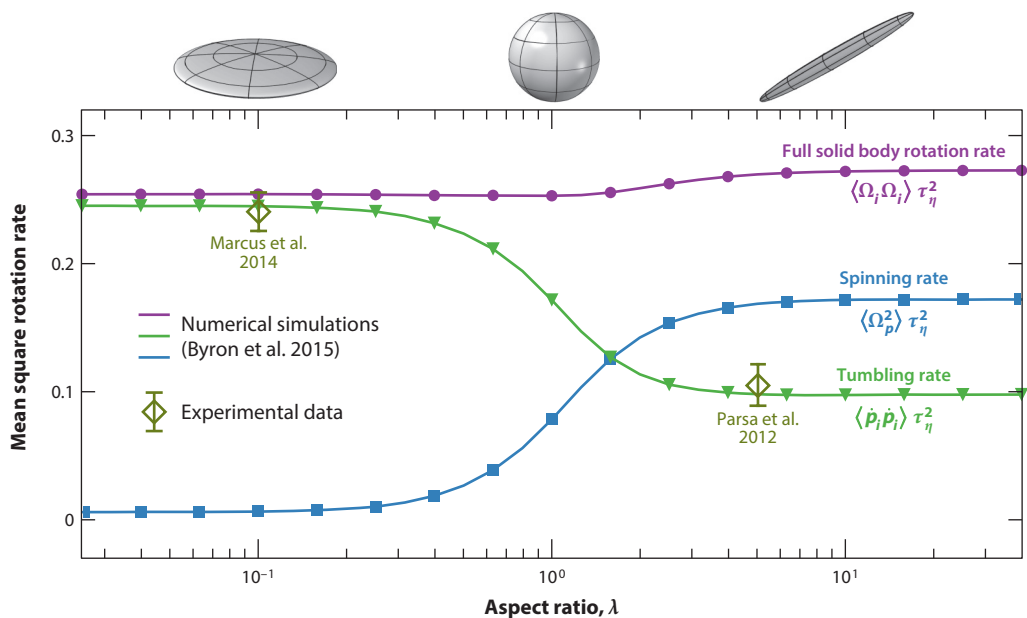


**Figure 8**

Mean square rotation rate as a function of aspect ratio for tracer particles in homogeneous isotropic turbulence.

## SETTLING DUE TO GRAVITY

Shape effects can modify the settling and growth rates of particles in relevant environmental phenomena, such as the formation of ice clouds (Pruppacher & Klett 2010) and the fallout and dispersion of volcanic ash (Beckett et al. 2015). The case of slender fibers sedimenting in a quiescent fluid has been considered in several studies reviewed by Guazzelli & Hinch (2011). This system displays an instability to clustering with rapid sedimentation of the clusters (Koch & Shaqfeh 1989). Inertial ellipsoids settling in a prototypical turbulent flow have been studied by Mallier & Maxey (1991). They demonstrated that both oblate and prolate spheroids fall faster than spheres in cellular flow. In recent DNS, Siewert et al. (2014a) observed that prolate and oblate ellipsoids in decaying isotropic turbulence settle faster than spherical particles. Siewert et al. (2014b) measured increased collision rates of the settling prolate and oblate ellipsoids compared to spherical particles of the same mass, attributing this phenomenon to the combined effects of preferential sweeping due to turbulence, increased settling velocity, and rotation.

### 6. SHAPE EFFECTS ON PARTICLE-TURBULENCE INTERACTIONS

The dynamics of many individual particles in turbulent flows combine to produce dramatic macroscopic effects. In many applications that motivate work in this field, the most pressing issues are these collective macroscopic phenomena. These are challenging problems given that modeling, simulating, or measuring many particles in turbulence at moderate to high concentrations is difficult. A number of phenomena could be included in this section, such as light scattering by aligned particles (Noel & Sassen 2005) and the rheology of fiber suspensions (Lundell et al. 2011). However, we review two problems that attracted the attention of researchers and for which significant progress has been made in connecting microscopic particle dynamics to the macroscopic phenomena of interest: preferential segregation and drag reduction. We also briefly discuss a few works focusing on anisotropic particles settling in isotropic turbulence due to its major importance in some environmental phenomena (see the sidebar Settling due to Gravity).

#### 6.1. Preferential Segregation in Bounded Flows

Preferential sweeping due to turbulence may cause nonuniformity in the fiber concentration and long-term segregation of fibers into specific flow regions. In wall-bounded flows, this can have consequences for the throughput of several industrial processes (Parsheh et al. 2005; Krochak et al. 2009, 2010; Carlsson et al. 2010; Håkansson et al. 2014). Interactions of inertial fibers with coherent structures near the wall make fibers segregate into elongated streaks, which correlate spatially with regions of low fluid velocity. This phenomenon has been observed on a qualitative basis by numerical simulation of inertial elongated ellipsoids modeled as pointwise particles (Zhang et al. 2001; Mortensen et al. 2008a,b).

**Figure 9** compares particle segregation from DNS data in a closed channel (Marchioli et al. 2010) with that from experimental data in an open channel (Håkansson et al. 2013, Kvick 2014). In **Figure 9a**, the streamwise fluid velocity fluctuations in the wall-parallel plane at  $z^+ = 6.4$  are superimposed to the position of pointwise fibers  $10z^+$  long. Fibers are gravity free with  $St = 30$  and  $\lambda = 50$ , but their finite length was ignored in the wall contact model. Fibers clearly segregate into the low-speed streaks. In **Figure 9b**, the position of fibers is captured from the transparent bottom of the channel. Fibers are slightly heavier than the fluid with  $\lambda = 28$ . Experiments show the same qualitative behavior of the DNS, with fibers clearly segregated into long streaks, the spacing of which indicates the typical distance between low-speed streaks in wall turbulence.

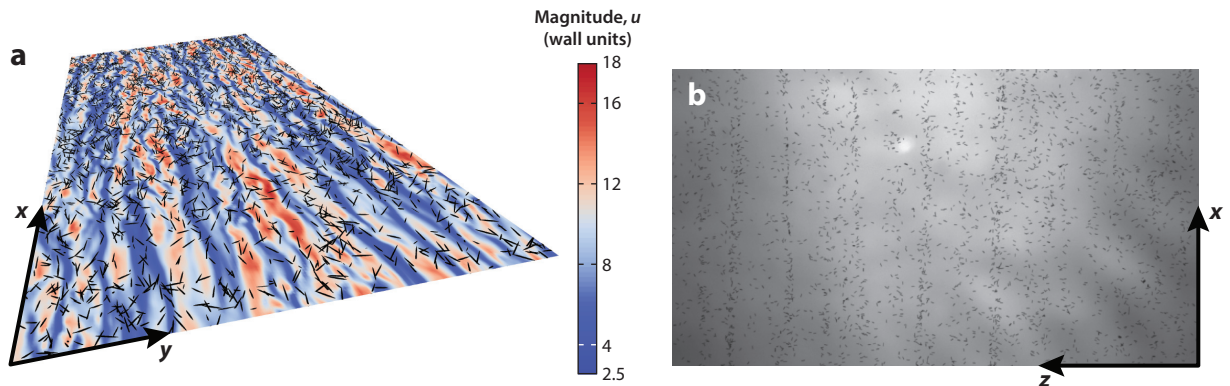


**Figure 9**

Fiber accumulation into low-speed streaks in turbulent channel flow. (a) Channel flow simulations at  $Re_\tau = 150$  (based on the half channel height) of inertial fibers  $10y^+$  long. (b) Experiments in an open channel at  $Re_\tau \simeq 178$  (based on the open channel height) of inertial fibers 1 mm long. Panel a adapted with permission from Marchioli et al. (2010), and panel b adapted with permission from Kvick (2014).

For increasing Reynolds number, the fibers show increasingly less segregation into streaks, possibly demonstrating an effect of wall interactions stronger than inertia. In a recent investigation, Challabotla et al. (2015a) reported a similar behavior for inertial oblate ellipsoids. In their DNS simulation of channel turbulence with four-way-coupled fiber dispersion, F. Zhao et al. (2015) observed that regardless of the aspect ratio and Stokes number, the tendency of prolate ellipsoids with small inertia to oversample low-speed streaks decreases for increasing  $\lambda$ , up to the point at which the average near-wall velocity of fibers increases beyond that of the fluid.

According to Do-Quang et al. (2014), this scenario can dramatically change if particles are fully resolved. With a DNS on the order of 10,000 spheroidal particles  $9.6z^+$  long, they studied a fully coupled turbulent flow laden with large particles with negligible inertia. **Figure 10** shows the position of fibers with a distance to the wall less than  $15z^+$ . Different from previous works, in the present case, particles have very small inertia, and it is possibly the combined effect of finite size and wall collisions that makes fibers segregate into high-speed streaks. Visualizations suggest that when the finite-size fibers are carried by a turbulent sweep toward the wall into a high-speed streak, wall interactions prevent them from following the fluid sideward into a low-speed streak. This result has implications for the mean streamwise velocity of particles, which in this case is larger than that of the fluid. An important consequence of particle preferential concentration by the structures of wall turbulence is the influence segregation has on settling and deposition phenomena. Soldati & Marchioli (2009), Zhang et al. (2001), and Marchioli et al. (2010) observed an increase of turbophoretic wall-normal velocity (Caporaloni et al. 1975) and settling for increasing aspect ratio. Similar trends have been reported for a quasi-DNS by Lecrivain et al. (2016).

## 6.2. Turbulent Drag Reduction

Understanding how turbulent drag can be influenced by the dispersion of small quantities of particles, and how the shape of such particles can be optimized, is an important issue for sustainable fluid transport (Procaccia et al. 2008). We examine the effects of small rigid, rod-like tracer fibers and of inertial ellipsoids on turbulence. Paschkewitz et al. (2004) used a finite-difference DNS of turbulence coupled with an Eulerian solver to compute the shear stress exerted on the fluid by rigid

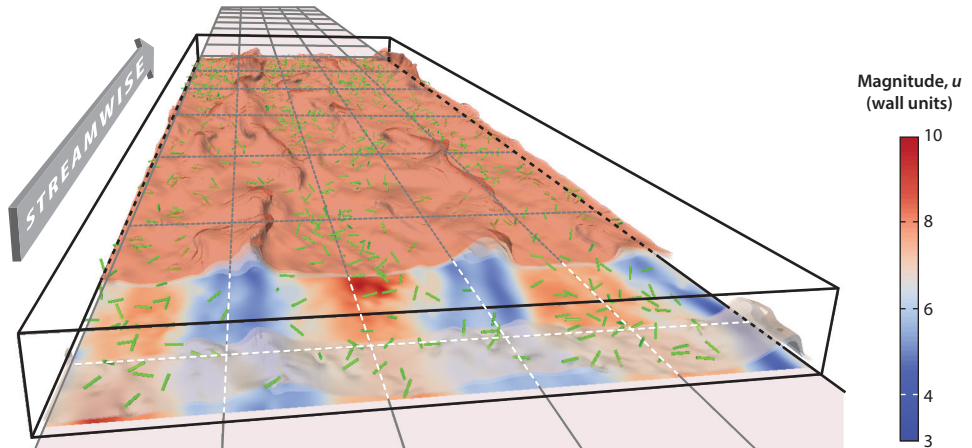


**Figure 10**

Fiber accumulation into high-speed streaks in turbulent channel flow. Simulations of inertial fibers  $10\gamma^+$  long are at  $Re_\tau = 150$ . Figure adapted with permission from Do-Quang et al. (2014).

rods much smaller than the Kolmogorov length scale. Rods, being small and at low concentration, are uniformly distributed but can apply stresses that depend on their orientation. **Figure 11a** illustrates the mechanism by which such tiny rods can reduce drag as proposed by Paschkewitz et al. (2004). These authors demonstrated that in the near-wall, turbulence-producing region of channel flow (Lumley & Blossey 1998), drag reduction correlates well with strong fluctuations of fiber stress in intervortex extensional regions. As a precursor to these intense fiber stress events, fibers align in the spanwise or wall-normal direction. Due to the intense fiber stress, the extensional

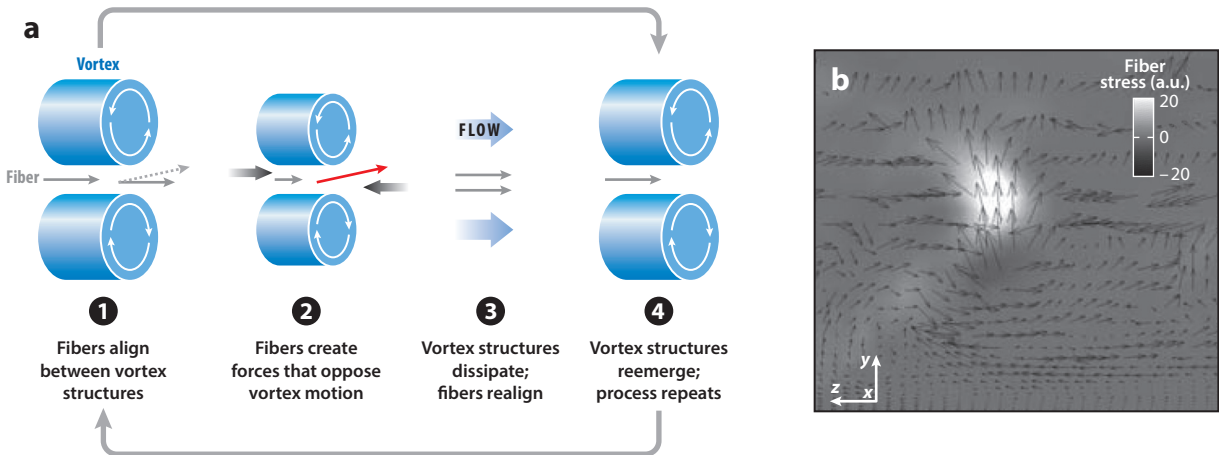


**Figure 11**

(a) Schematic illustration of the mechanism for fiber-induced drag reduction. **1** Fibers align in intervortex regions. **2** Fibers generate large stresses and body forces that oppose vortex motion. **3** Vortex structures are dissipated, and fibers realign in the flow direction. **4** Vortex structures reemerge, and the cycle repeats. (b) Cross-stream snapshot of the instantaneous wall-normal component of the fiber stress superimposed on the projection of the primary orientation axis vector. Figure adapted with permission from Paschkewitz et al. (2004).

flow is progressively reduced down to a level that allows fibers to realign into the flow streamwise direction so that the fiber stress is also reduced. Correspondingly, the vortices are weakened or destroyed (Paschkewitz et al. 2005b).

**Figure 11b** shows the correlation of the extra shear stress and the orientation of the fibers, with the color map of the wall-normal component of the fiber stress acting on the fluid superimposed with the cross-stream projection of the primary axis orientation of fibers. In a channel with a shear Reynolds number of 150, Paschkewitz et al. (2004) computed drag reduction up to 26%, whereas companion experimental measurements (Paschkewitz et al. 2005a) demonstrated a more modest value of 10%. Within the limit of fibers much smaller than the Kolmogorov scale, similar observations were made by Gillissen et al. (2008). Moosaie (2013) and Moosaie & Manhart (2015) confirmed the drag reduction mechanisms by tiny fibers and have been able to compute drag reduction up to 16% in a channel flow at  $Re_\tau = 180$ .

A different mechanism by which the turbulence-regeneration cycle can be weakened occurs in the case of inertial particles. Simulations have shown that the tendency of small inertial particles to segregate into low-speed streaks is associated with the modulation of turbulence statistics and drag reduction (Pan & Banerjee 1996, Dritselis & Vlachos 2008, Zhao et al. 2010). Recent Eulerian-Lagrangian simulations of inertial spheroids in turbulent channel flow have also shown similar effects. Andersson et al. (2012) performed a two-way-coupled Eulerian-Lagrangian DNS of 2.5 million inertial pointwise spheres and  $\lambda = 5$  ellipsoids interacting with turbulence in channel flow. Compared to the usual force-coupled simulations (Squires & Eaton 1990, Crowe et al. 1996), they used force and torque coupling between ellipsoids and the fluid and were able to demonstrate drag reduction for both spheres and ellipsoids. However, they also reported that in force- and torque-coupled simulations, turbulence modulation effects decreased compared with the case in which only force coupling is accounted for. L. Zhao et al. (2015) observed that interparticle and particle-wall collisions can be important in particle-laden flows, particularly in the wall region, where the particle concentration can also reach locally high values in flows that are dilute on average. They performed Eulerian-Lagrangian four-way-coupled simulations considering pointwise spheres and inertial fibers. They confirmed that inertial ellipsoids segregate into low-speed streaks, add inertia, and delay all fluid motions in the wall region, thus changing the synchronization of the wall turbulence-regeneration cycle. L. Zhao et al. (2015) reported a maximum drag reduction of approximately 5% obtained for fibers with  $\lambda = 5$ , which reduce drag significantly more than spheres. Do-Quang et al. (2014) qualitatively observed the decrease in wall turbulence structures associated with a reduced intensity of the streamwise fluctuations by studying turbulent channel flow at  $Re_\tau = 180$  of a low concentration of large elongated particles with small Stokes number and size up to 24 wall units.

## SUMMARY POINTS

1. Anisotropic particles occur in a dazzling variety of shapes. The case of rigid spheroidal particles is mathematically tractable and allows insights into the many ways nonspherical shape is important to particle dynamics in turbulence. Particles of many other shapes can be treated as ellipsoids with effective aspect ratios.
2. The number of parameters needed to fully specify a turbulent flow with nonspherical particles is large. A phenomenology of the simple foundational case of small spheroidal particles at low concentrations in canonical flows has been developed, but many other parts of the large parameter space have barely been explored.

3. Small particles behave like tracers with translation that matches the fluid and rotation that has the same contribution from vorticity as the fluid with an additional contribution from the strain rate. Small slender fibers rotate like material lines. Because particles rotate in response to the small scales in turbulent flows, nonspherical particle dynamics have a degree of universality that reflects the common features of small-scale turbulence.
4. Point-particle models for inertial nonspherical particles in the Stokes drag regime have been rigorously derived and are widely used. When fluid inertia becomes important, models are available that rely on empirical expressions for drag, lift, and unsteady effects. In the slender fiber limit, we have the most comprehensive set of models, extending from point particles to fibers longer than the Kolmogorov scale.
5. DNS of anisotropic particles in turbulence are increasingly available and have produced a wealth of data and insights, mostly for tracers and inertial point particles. Rapid progress is extending DNS to complex flows, turbulence modulation, large particles, and other frontiers.
6. Experimental techniques for imaging the dynamics of individual nonspherical particles in a turbulent environment have recently become available.
7. In homogeneous isotropic turbulence, fibers spin much faster than they tumble, whereas disks tumble much faster than they spin. The combined solid-body rotation rate is nearly independent of shape. These effects can be understood as a consequence of a particle aligning with a long axis parallel to the vorticity as a consequence of Lagrangian stretching in the flow.
8. The alignment of spheroids in turbulent channel flow displays a rich phenomenology. Prolate ellipsoids align with their symmetry axis in the streamwise direction, whereas the alignment of oblate ellipsoids depends on their inertia, with tracers aligning in the wall-normal direction and heavy disks aligning in the spanwise direction.
9. Inertial fibers and tracers can alter turbulence-regeneration mechanisms in different ways: Rigid, inertia-less fibers can produce extra stresses, damping the counter-rotating vortices in the wall region and producing drag reduction. Inertial fibers can segregate preferentially into low-speed streaks and delay the fluid flow.

## FUTURE ISSUES

1. Macroscopic consequences of individual particle dynamics are only partly understood, with large proportions of parameter space to be explored and many aspects of the complex cases relevant to applications still to be grounded in fundamental physics.
2. **Figure 3** identifies some classes of models that have been used. Point-particle models that rigorously account for effects of fluid inertia in the unsteady case relevant to turbulence do not exist for shapes other than spheres and slender bodies. Development of these models and quantification of the parameters at which various models can reliably be used for specific quantities would be valuable.

3. Numerical simulations capable of handling arbitrarily shaped particles in turbulence are needed. Stokesian dynamics and lattice Boltzmann methods can be used. However, simulations that resolve turbulence scales and particle scales while acquiring sufficient statistics to achieve convergence are computationally expensive.
4. A particular need in experiments is the ability to track individual particles at higher concentrations, at which drag reduction and changes in suspension rheology become important.
5. Careful attention needs to be given to the effects of inhomogeneity of the turbulent flow on nonspherical particle motion. Inertial particles in inhomogeneous flows carry a memory of the region of the flow they recently came from (Gerashchenko et al. 2008). Predictive understanding of inhomogeneous flows with nonspherical inertial particles will require models capable of accounting for the Lagrangian history of particles and of fluid velocity gradients.
6. The case of active matter made of self-propelled particles provides another interesting class of nonspherical particle motion (Lauga 2016), and the study of active nonspherical particles in turbulence is promising.

## DISCLOSURE STATEMENT

The authors are not aware of any biases that might be perceived as affecting the objectivity of this review.

## ACKNOWLEDGMENTS

The authors thank colleagues who allowed the use of their images in this review and all those who provided advice and suggestions on the manuscript. G.A.V. acknowledges support from NSF grant DMR-1508575 and Army Research Office grant W911NF-15-1-0205. The authors are grateful to the European Cooperation in Science and Technology (COST), action number FP 1005 on *Fibre suspension flow modeling*.

## LITERATURE CITED

- Abbasi Hoseini A, Zavareh Z, Lundell F, Anderson HI. 2014. Rod-like particles matching algorithm based on SOM neural network in dispersed two-phase flow measurements. *Exp. Fluids* 55:1705
- Aidun CK, Clausen JR. 2010. Lattice-Boltzmann method for complex flows. *Annu. Rev. Fluid Mech.* 42:439–72
- Andersson HI, Zhao L, Barri M. 2012. Torque-coupling and particle–turbulence interactions. *J. Fluid Mech.* 696:319–29
- Arribas M, Elipe A, Palacios M. 2006. Quaternions and the rotation of a rigid body. *Celest. Mech. Dyn. Astron.* 96:239–51
- Balachandar S, Eaton JK. 2010. Turbulent dispersed multiphase flow. *Annu. Rev. Fluid Mech.* 42:111–33
- Beckett F, Witham C, Hort M, Stevenson J, Bonadonna C, Millington S. 2015. Sensitivity of dispersion model forecasts of volcanic ash clouds to the physical characteristics of the particles. *J. Geophys. Res. Atmos.* 120:11636–52
- Bellani G, Byron ML, Collignon AG, Meyer CR, Variano EA. 2012. Shape effects on turbulent modulation by large nearly neutrally buoyant particles. *J. Fluid Mech.* 712:41–60

- Bellani G, Nole MA, Variano EA. 2013. Turbulence modulation by large ellipsoidal particles: concentration effects. *Acta Mech.* 224:2291–99
- Bernstein O, Shapiro M. 1994. Direct determination of the orientation distribution function of cylindrical particles immersed in laminar and turbulent shear flows. *J. Aerosol. Sci.* 25:113–36
- Bianco F, Chibbaro S, Marchioli C, Salvetti MV, Soldati A. 2012. Intrinsic filtering errors of Lagrangian particle tracking in LES flow fields. *Phys. Fluids* 24:045103
- Bird RB, Stewart WE, Lightfoot EN. 1960. *Transport Phenomena*. New York: Wiley
- Brenner H. 1963. The Stokes resistance of an arbitrary particle. *Chem. Eng. Sci.* 18:1–25
- Brenner H. 1964a. The Stokes resistance of an arbitrary particle—II. An extension. *Chem. Eng. Sci.* 19:599–629
- Brenner H. 1964b. The Stokes resistance of an arbitrary particle—III. Shear fields. *Chem. Eng. Sci.* 19:631–51
- Brenner H. 1964c. The Stokes resistance of an arbitrary particle—IV. Arbitrary fields of flow. *Chem. Eng. Sci.* 19:703–27
- Bretherton FP. 1962. The motion of rigid particles in a shear flow at low Reynolds number. *J. Fluid Mech.* 14:284–304
- Brown RD, Warhaft Z, Voth GA. 2009. Acceleration statistics of neutrally buoyant spherical particles in intense turbulence. *Phys. Rev. Lett.* 103:194501
- Byron M, Einarsson J, Gustavsson K, Voth G, Mehlig B, Variano E. 2015. Shape-dependence of particle rotation in isotropic turbulence. *Phys. Fluids* 27:035101
- Calzavarini E, Volk R, Bourgoin M, Leveque E, Pinton JF, Toschi F. 2009. Acceleration statistics of finite-sized particles in turbulent flow: the role of Faxén forces. *J. Fluid Mech.* 630:179–89
- Capone A, Romano GP. 2015. Interactions between fluid and fibers in a turbulent backward-facing step flow. *Phys. Fluids* 27:053303
- Capone A, Romano GP, Soldati A. 2015. Experimental investigation on interactions among fluid and rod-like particles in a turbulent pipe jet by means of particle image velocimetry. *Exp. Fluids* 56:1
- Caporaloni M, Tampieri F, Trombetti F, Vittori O. 1975. Transfer of particles in nonisotropic air turbulence. *J. Atmos. Sci.* 32:565–68
- Carlsson A, Håkansson K, Kvick M, Lundell F, Söderberg LD. 2011. Evaluation of steerable filter for detection of fibers in flowing suspensions. *Exp. Fluids* 51:987–96
- Carlsson A, Soderberg L, Lundell F. 2010. Fibre orientation measurements near a headbox wall. *Nord. Pulp Pap. Res. J.* 25:204–12
- Challabotla NR, Zhao L, Andersson HI. 2015a. Orientation and rotation of inertial disk particles in wall turbulence. *J. Fluid Mech.* 766:R2
- Challabotla NR, Zhao L, Andersson HI. 2015b. Shape effects on dynamics of inertia-free spheroids in wall turbulence. *Phys. Fluids* 27:061703
- Chen J, Jin G, Zhang J. 2016. Large eddy simulation of orientation and rotation of ellipsoidal particles in isotropic turbulent flows. *J. Turbul.* 17:308–26
- Chevillard L, Meneveau C. 2013. Orientation dynamics of small, triaxial-ellipsoidal particles in isotropic turbulence. *J. Fluid Mech.* 737:571–96
- Crowe CT, Troutt R, Chung N. 1996. Two-phase turbulent flows. *Annu. Rev. Fluid Mech.* 28:11–43
- Dearing SS, Campolo M, Capone A, Soldati A. 2013. Phase discrimination and object fitting to measure fibers distribution and orientation in turbulent pipe flows. *Exp. Fluids* 54:1419
- Den Toonder J, Hulsen M, Kuiken G, Nieuwstadt F. 1997. Drag reduction by polymer additives in a turbulent pipe flow: numerical and laboratory experiments. *J. Fluid Mech.* 337:193–231
- Ding EJ, Aidun CK. 2000. The dynamics and scaling law for particles suspended in shear flow with inertia. *J. Fluid Mech.* 423:317–44
- Do-Quang M, Amberg G, Brethouwer G, Johansson AV. 2014. Simulation of finite-size fibers in turbulent channel flows. *Phys. Rev. E* 89:013006
- Dritselis CD, Vlachos NS. 2008. Numerical study of educed coherent structures in the near-wall region of a particle-laden channel flow. *Phys. Fluids* 20:055103
- Einarsson J. 2015. *Angular dynamics of small particles in fluids*. PhD Thesis, Univ. Gothenburg
- Einarsson J, Candelier F, Lundell F, Angilella JR, Mehlig B. 2015. Rotation of a spheroid in a simple shear at small Reynolds number. *Phys. Fluids* 27:063301

- El Khoury GK, Andersson HI, Pettersen B. 2010. Crossflow past a prolate spheroid at Reynolds number of 10,000. *J. Fluid Mech.* 659:365–74
- Elghobashi S, Prosperetti A. 2009. Point-particle model for disperse turbulent flows. *Int. J. Multiphase Flow* 35:791–878
- Erni P, Cramer C, Marti I, Windhab EJ, Fischer P. 2009. Continuous flow structuring of anisotropic biopolymer particles. *Adv. Colloid Interface Sci.* 150:16–26
- Ganser GH. 1993. A rational approach to drag prediction of spherical and nonspherical particles. *Powder Technol.* 77:143–52
- Gatignol R. 1983. The Faxen formulas for a rigid particle in an unsteady non-uniform Stokes flow. *J. Mech. Theor. Appl.* 2:143–60
- Gerashchenko S, Sharp NS, Neuscammen S, Warhaft Z. 2008. Lagrangian measurements of inertial particle accelerations in a turbulent boundary layer. *J. Fluid Mech.* 617:255–81
- Geurts BJ, Kuerten JGM. 2012. Ideal stochastic forcing for the motion of particles in large-eddy simulation extracted from direct numerical simulation of turbulent channel flow. *Phys. Fluids* 24:081702
- Gillissen JJJ, Boersma BJ, Mortensen PH, Andersson HI. 2007a. On the performance of the moment approximation for the numerical computation of fiber stress in turbulent channel flow. *Phys. Fluids* 19:035102
- Gillissen JJJ, Boersma BJ, Mortensen PH, Andersson HI. 2007b. The stress generated by non-Brownian fibers in turbulent channel flow simulations. *Phys. Fluids* 19:115107
- Gillissen JJJ, Boersma BJ, Mortensen PH, Andersson HI. 2008. Fibre-induced drag reduction. *J. Fluid Mech.* 602:209–18
- Guazzelli É, Hinch J. 2011. Fluctuations and instability in sedimentation. *Annu. Rev. Fluid Mech.* 43:97–116
- Guazzelli É, Morris JF. 2012. *A Physical Introduction to Suspension Dynamics*. Cambridge, UK: Cambridge Univ. Press
- Gustavsson K, Einarsson J, Mehlig B. 2014. Tumbling of small axisymmetric particles in random and turbulent flows. *Phys. Rev. Lett.* 112:014501
- Haider A, Levenspiel O. 1989. Drag coefficients and terminal velocity of spherical and nonspherical particles. *Powder Technol.* 58:63–70
- Håkansson KMO, Fall AB, Lundell F, Yu S, Krywka C, et al. 2014. Hydrodynamic alignment and assembly of nanofibrils resulting in strong cellulose filaments. *Nat. Commun.* 5:4018
- Håkansson KMO, Kvick M, Lundell F, Prahl Wittberg L, Söderberg LD. 2013. Measurement of width and intensity of particle streaks in turbulent flows. *Exp. Fluids* 54:1555
- Harris JB, Pittman JFT. 1975. Equivalent ellipsoidal axis ratios of slender rod-like particles. *J. Colloid Interface Sci.* 50:280–82
- Heymsfield AJ. 1977. Precipitation development in stratiform ice clouds: a microphysical and dynamical study. *J. Atmos. Sci.* 34:367–81
- Hinch EJ, Leal LG. 1972. The effect of Brownian motion on the rheological properties of a suspension of non-spherical particles. *J. Fluid Mech.* 52:683–712
- Hinch EJ, Leal LG. 1975. Constitutive equations in suspension mechanics. Part 2. Approximate forms for a suspension. *J. Fluid Mech.* 76:187–208
- Holm R, Soderberg D. 2007. Shear influence on fibre orientation: dilute suspension in the near wall region. *Rheol. Acta* 46:721–29
- Hölzer A, Sommerfeld M. 2008. New simple correlation formula for the drag coefficient of non-spherical particles. *Powder Technol.* 184:361–65
- Hoseini AA, Lundell F, Andersson HI. 2015. Finite-length effects on dynamical behavior of rod-like particles in wall-bounded turbulent flow. *Int. J. Multiphase Flow* 76:13–21
- Hussain AKMF. 1983. Coherent structures—reality and myth. *Phys. Fluids* 26:2816–50
- Jeffery GB. 1922. The motion of ellipsoidal particles immersed in a viscous fluid. *Proc. R. Soc. Lond. A* 102:161–79
- Jiang F, Gallardo JP, Andersson HI. 2014. The laminar wake behind a 6:1 prolate spheroid at 45° incidence angle. *Phys. Fluids* 26:113602
- Jiang F, Gallardo JP, Andersson HI, Zhang Z. 2015. The transitional wake behind an inclined prolate spheroid. *Phys. Fluids* 27:093602

- Khayat RE, Cox RG. 1989. Inertia effects on the motion of long slender bodies. *J. Fluid Mech.* 209:435–62
- Kim S, Karrila SJ. 1991. *Microhydrodynamics: Principles and Selected Applications*. Boston: Butterworth-Heinemann
- Koch DL, Shaqfeh ESG. 1989. The instability of a dispersion of sedimenting spheroids. *J. Fluid Mech.* 209:521–42
- Kramel S, Tympel S, Toschi F, Voth GA. 2016. Preferential rotation of chiral dipoles in isotropic turbulence. arXiv:1602.07413v1 [physics.flu-dyn]
- Krochak PJ, Olson JA, Martinez DM. 2009. Fiber suspension flow in a tapered channel: the effect of flow/fiber coupling. *Int. J. Multiphase Flow* 35:676–88
- Krochak PJ, Olson JA, Martinez DM. 2010. Near-wall estimates of the concentration and orientation distribution of a semi-dilute rigid fibre suspension in Poiseuille flow. *J. Fluid Mech.* 653:431–62
- Krushkal EM, Gallily I. 1988. On the orientation distribution function of non-spherical aerosol particles in a general shear flow—II. The turbulent case. *J. Aerosol. Sci.* 19:197–211
- Kvick M. 2014. *Transitional and turbulent fibre suspension flows*. PhD Thesis, R. Inst. Technol., KTH, Stockholm
- Lapple CE, Shepherd CB. 1940. Calculation of particle trajectories. *Ind. Eng. Chem. Res.* 32:605–17
- Lauga E. 2016. Bacterial hydrodynamics. *Annu. Rev. Fluid Mech.* 48:105–30
- Lecrivain G, Rayan R, Hurtado A, Hampel U. 2016. Using quasi-DNS to investigate the deposition of elongated aerosol particles in a wavy channel flow. *Comput. Fluids* 124:78–85
- Leith D. 1987. Drag on nonspherical objects. *Aerosol Sci. Technol.* 6:153–61
- Liu D, Keaveny EE, Maxey MR, Karniadakis GE. 2009. Force-coupling method for flows with ellipsoidal particles. *J. Comput. Phys.* 228:3559–81
- Loth E. 2008. Drag of non-spherical solid particles of regular and irregular shape. *Powder Technol.* 182:342–53
- Lucci F, Ferrante A, Elghobashi S. 2010. Modulation of isotropic turbulence by particles of Taylor length-scale size. *J. Fluid Mech.* 650:5–55
- Lumley J, Blossey P. 1998. Control of turbulence. *Annu. Rev. Fluid Mech.* 30:311–27
- Lundell F, Söderberg LD, Alfredsson PH. 2011. Fluid mechanics of papermaking. *Annu. Rev. Fluid Mech.* 43:195–217
- Mallier R, Maxey M. 1991. The settling of nonspherical particles in a cellular flow field. *Phys. Fluids A* 3:1481–94
- Mandø M, Rosendahl L. 2010. On the motion of non-spherical particles at high Reynolds number. *Powder Technol.* 202:1–13
- Marchioli C, Fantoni M, Soldati A. 2010. Orientation, distribution, and deposition of elongated, inertial fibers in turbulent channel flow. *Phys. Fluids* 22:033301
- Marchioli C, Soldati A. 2013. Rotation statistics of fibers in wall shear turbulence. *Acta Mech.* 224:2311–29
- Marchioli C, Zhao L, Andersson HI. 2016. On the relative rotational motion between rigid fibers and fluid in turbulent channel flow. *Phys. Fluids* 28:013301
- Marcus GG, Parsa S, Kramel S, Ni R, Voth GA. 2014. Measurements of the solid-body rotation of anisotropic particles in 3D turbulence. *New J. Phys.* 16:102001
- Maxey MR. 1983. Equation of motion for a small rigid sphere in a nonuniform flow. *Phys. Fluids* 26:883–88
- Meller Y, Liberzon A. 2015. Particle-fluid interaction forces as the source of acceleration PDF invariance in particle size. *Int. J. Multiphase Flow* 76:22–31
- Meneveau C. 2011. Lagrangian dynamics and models of the velocity gradient tensor in turbulent flows. *Annu. Rev. Fluid Mech.* 43:219–45
- Mittal R, Iaccarino G. 2005. Immersed boundary methods. *Annu. Rev. Fluid Mech.* 37:239–61
- Moffett RC, Prather KA. 2009. In-situ measurements of the mixing state and optical properties of soot with implications for radiative forcing estimates. *PNAS* 106:11872–77
- Moin P, Mahesh K. 1998. Direct numerical simulation: a tool in turbulence research. *Annu. Rev. Fluid Mech.* 30:539–78
- Moosaie A. 2013. Effect of rotary inertia on the orientational behavior of dilute Brownian and non-Brownian fiber suspensions. *J. Dispers. Sci. Technol.* 34:70–79
- Moosaie A, Manhart M. 2011. An algebraic closure for the DNS of fiber-induced turbulent drag reduction in a channel flow. *J. Non-Newton. Fluid Mech.* 166:1190–97

- Moosaie A, Manhart M. 2015. On the structure of vorticity and near-wall partial enstrophy in fibrous drag-reduced turbulent channel flow. *J. Non-Newton. Fluid Mech.* 223:249–56
- Mortensen PH, Andersson HI, Gillissen JJJ, Boersma BJ. 2008a. Dynamics of prolate ellipsoidal particles in a turbulent channel flow. *Phys. Fluids* 20:093302
- Mortensen PH, Andersson HI, Gillissen JJJ, Boersma BJ. 2008b. On the orientation of ellipsoidal particles in a turbulent shear flow. *Int. J. Multiphase Flow* 34:678–83
- Ni R, Kramel S, Ouellette NT, Voth GA. 2015. Measurements of the coupling between the tumbling of rods and the velocity gradient tensor in turbulence. *J. Fluid Mech.* 766:202–25
- Ni R, Ouellette NT, Voth GA. 2014. Alignment of vorticity and rods with Lagrangian fluid stretching in turbulence. *J. Fluid Mech.* 743:R3
- Njobuenwu DO, Fairweather M. 2015. Dynamics of single, non-spherical ellipsoidal particles in a turbulent channel flow. *Chem. Eng. Sci.* 123:265–82
- Noel V, Sassen K. 2005. Study of planar ice crystal orientations in ice clouds from scanning polarization lidar observations. *J. Appl. Meteorol.* 44:653–64
- Olson JA, Kerekes RJ. 1998. The motion of fibres in turbulent flow. *J. Fluid Mech.* 377:47–64
- Ouchene R, Khalij M, Tanière A, Arcen B. 2015. Drag, lift and torque coefficients for ellipsoidal particles: from low to moderate particle Reynolds numbers. *Comput. Fluids* 113:53–64
- Pan TW, Glowinski R, Galdi GP. 2002. Direct simulation of the motion of a settling ellipsoid in Newtonian fluid. *J. Comput. Appl. Math.* 149:71–82
- Pan Y, Banerjee S. 1996. Numerical simulation of particle interactions with wall turbulence. *Phys. Fluids* 8:2733–55
- Parsa S, Calzavarini E, Toschi F, Voth GA. 2012. Rotation rate of rods in turbulent fluid flow. *Phys. Rev. Lett.* 109:134501
- Parsa S, Voth GA. 2014. Inertial range scaling in rotations of long rods in turbulence. *Phys. Rev. Lett.* 112:024501
- Parshah M, Brown ML, Aidun CK. 2005. On the orientation of stiff fibres suspended in turbulent flow in a planar contraction. *J. Fluid Mech.* 545:245–69
- Parshah M, Brown ML, Aidun CK. 2006. Variation of fiber orientation in turbulent flow inside a planar contraction with different shapes. *Int. J. Multiphase Flow* 32:1354–69
- Paschkewitz JS, Dimitropoulos CD, Hou YX, Somandepalli VSR, Mungal MG, et al. 2005a. An experimental and numerical investigation of drag reduction in a turbulent boundary layer using a rigid rodlike polymer. *Phys. Fluids* 17:085101
- Paschkewitz JS, Dubief Y, Dimitropoulos CD, Shaqfeh ESG, Moin P. 2004. Numerical simulation of turbulent drag reduction using rigid fibres. *J. Fluid Mech.* 518:281–317
- Paschkewitz JS, Dubief Y, Shaqfeh ESG. 2005b. The dynamic mechanism for turbulent drag reduction using rigid fibers based on Lagrangian conditional statistics. *Phys. Fluids* 17:063102
- Pedley TJ, Kessler JO. 1992. Hydrodynamic phenomena in suspensions of swimming microorganisms. *Annu. Rev. Fluid Mech.* 24:313–58
- Procaccia I, L'vov VS, Benzi R. 2008. Colloquium: theory of drag reduction by polymers in wall-bounded turbulence. *Rev. Mod. Phys.* 80:225
- Pruppacher HR, Klett JD. 2010. *Microphysics of Clouds and Precipitation*. Dordrecht: Kluwer Acad. 2nd ed.
- Pumir A, Wilkinson M. 2011. Orientation statistics of small particles in turbulence. *New J. Phys.* 13:093030
- Raman V, Fox RO. 2016. Modeling of fine-particle formation in turbulent flames. *Annu. Rev. Fluid Mech.* 48:159–90
- Rogallo RS, Moin P. 1984. Numerical simulation of turbulent flows. *Annu. Rev. Fluid Mech.* 16:99–137
- Rosén T, Einarsson J, Nordmark A, Aidun CK, Lundell F, Mehlig B. 2015. Numerical analysis of the angular motion of a neutrally buoyant spheroid in shear flow at small Reynolds numbers. *Phys. Rev. E* 92:063022
- Rosendahl L. 2000. Using a multi-parameter particle shape description to predict the motion of non-spherical particle shapes in swirling flow. *Appl. Math. Model.* 24:11–25
- Sabban L, van Hout R. 2011. Measurements of pollen grain dispersal in still air and stationary, near homogeneous, isotropic turbulence. *J. Aerosol Sci.* 42:867–82
- Shapiro M, Goldenberg M. 1993. Deposition of glass fiber particles from turbulent air flow in a pipe. *J. Aerosol Sci.* 24:65–87

- Shin H, Maxey MR. 1997. Chaotic motion of nonspherical particles settling in a cellular flow field. *Phys. Rev. E* 56:5431–44
- Shin M, Koch DL. 2005. Rotational and translational dispersion of fibres in isotropic turbulent flows. *J. Fluid Mech.* 540:143–74
- Siewert C, Kunnen RPJ, Meinke M, Schröder W. 2014a. Orientation statistics and settling velocity of ellipsoids in decaying turbulence. *Atmos. Res.* 142:45–56
- Siewert C, Kunnen RPJ, Schröder W. 2014b. Collision rates of small ellipsoids settling in turbulence. *J. Fluid Mech.* 758:686–701
- Soldati A, Andersson HI. 2013. Anisotropic particles in turbulence: status and outlook. *Acta Mech.* 224:2219–23
- Soldati A, Marchioli C. 2009. Physics and modelling of turbulent particle deposition and entrainment: review of a systematic study. *Int. J. Multiphase Flow* 35:827–39
- Squires KD, Eaton JK. 1990. Particle response and turbulence modification in isotropic turbulence. *Phys. Fluids A* 2:1191–203
- Subramanian G, Koch DL. 2005. Inertial effects on fibre motion in simple shear flow. *J. Fluid Mech.* 535:383–414
- Suen JKC, Joo YL, Armstrong RC. 2002. Molecular orientation effects in viscoelasticity. *Annu. Rev. Fluid Mech.* 34:417–44
- Szeri AJ. 1993. Pattern formation in recirculating flows of suspensions of orientable particles. *Philos. Trans. Phys. Sci. Eng.* 345:477–506
- Szeri AJ, Leal LG. 1992. A new computational method for the solution of flow problems of microstructured fluids. Part 1: theory. *J. Fluid Mech.* 242:549–76
- Szeri AJ, Leal LG. 1993. Microstructure suspended in three-dimensional flows. *J. Fluid Mech.* 250:143–67
- Szeri AJ, Leal LG. 1994. A new computational method for the solution of flow problems of microstructured fluids. Part 2: inhomogeneous shear flow of a suspension. *J. Fluid Mech.* 262:171–204
- Tenneti S, Subramaniam S. 2014. Particle-resolved direct numerical simulation for gas-solid flow model development. *Annu. Rev. Fluid Mech.* 46:199–230
- Toschi F, Bodenschatz E. 2009. Lagrangian properties of particles in turbulence. *Annu. Rev. Fluid Mech.* 41:375–404
- Uhlmann M. 2008. Interface-resolved direct numerical simulation of vertical particulate channel flow in the turbulent regime. *Phys. Fluids* 20:53305
- van Hout R, Sabban L, Cohen A. 2013. The use of high-speed PIV and holographic cinematography in the study of fiber suspension flows. *Acta Mech.* 224:2263–80
- Voth GA. 2015. Disks aligned in a turbulent channel. *J. Fluid Mech.* 772:1–4
- Wilkinson M, Bezuglyy V, Mehlig B. 2010. Emergent order in rheoscopic swirls. *J. Fluid Mech.* 667:158–87
- Yin C, Rosendahl L, Knudsen SK, Henrik S. 2003. Modelling the motion of cylindrical particles in a nonuniform flow. *Chem. Eng. Sci.* 58:3489–98
- Zastawny M, Mallouppas G, Zhao F, van Wachem B. 2012. Derivation of drag and lift force and torque coefficients for non-spherical particles in flows. *Int. J. Multiphase Flow* 39:227–39
- Zhang H, Ahmadi G, Fan FG, McLaughlin JB. 2001. Ellipsoidal particle transport and deposition in turbulent channel flows. *Int. J. Multiphase Flow* 27:971–1009
- Zhao F, George WK, van Wachem BGM. 2015. Four-way coupled simulations of small particles in turbulent channel flow: the effects of particle shape and Stokes number. *Phys. Fluids* 27:083301
- Zhao F, van Wachem B. 2013. Direct numerical simulation of ellipsoidal particles in turbulent channel flow. *Acta Mech.* 224:2331–58
- Zhao L, Andersson HI, Gillissen J. 2010. Turbulence modulation and drag reduction by spherical particles. *Phys. Fluids* 22:081702
- Zhao L, Challabotla NR, Andersson HI, Variano EA. 2015. Rotation of nonspherical particles in turbulent channel flow. *Phys. Rev. Lett.* 115:244501